RECONSTRUCTING SEASONAL TEMPERATURE AND SALINITY IN THE MID TO HIGH LATITUDES OF THE PERMIAN USING BRACHIOPOD SHELL $\delta^{18}O$

A Thesis

by

MEAGAN ELIZABETH DEPUGH

Submitted to the Office of Graduate and Professional Studies of
Texas A&M University
in partial fulfillment of the requirements for the degree of

MASTER OF SCIENCE

Chair of Committee,	Ethan L. Grossman
Committee Members,	Brendan Roark
	Juan Carlos Laya
	Thomas Yancey
Head of Department,	Michael C. Pope

August 2019

Major Subject: Geology

ABSTRACT

We used oxygen and carbon isotopic compositions of Permian-aged brachiopods from Argentina, Western Australia, Arctic Canada, and West Spitsbergen to create high-resolution snapshots of the seasonal temperature and salinity patterns experienced by these mid- to high-latitudes and provide an in-depth peek at climates past.

Brachiopods were examined in thin section and under cathodoluminescence to evaluate preservation and were milled along visible growth-associated banding to produce isotopic records that correspond with annual growth cycles of the specimens. The resulting $\delta^{18}O$ records generally exhibited systematic, cyclic variation across the specimen that are interpreted as seasonal changes in environmental conditions over the lifetime of the specimen.

The isotopic records of the brachiopod shells vary with age and location. The Asselian-aged Argentinian brachiopod has consistently low $\delta^{18}O$ and $\delta^{13}C$ values. The seasonal variability in $\delta^{18}O$ was -4.6‰ to -5.4‰, which corresponds to a 4ºC range in annual temperature (assuming no seasonal variation in seawater $\delta^{18}O$ and thus salinity). Western Australian brachiopods, which are Sakmarian to Artinskian in age, yield the highest $\delta^{18}O$ values of the study, equivalent to a comparable annual temperature range of 5ºC, but with substantially higher $\delta^{18}O$ values (0.2‰ to -1.0‰). Arctic Canada brachiopods yield the smallest range in annual temperature, equal to 3ºC, and have moderately high $\delta^{18}O$ and $\delta^{13}C$ values. These Roadian shells are of the same age as the Spitsbergen shells, but their records are considerably dissimilar. Spitsbergen shells

provide the lowest $\delta^{18}O$ values, the highest $\delta^{13}C$ values, the highest seasonal range in $\delta^{18}O$ (-3.7‰ to -6.2‰), and thus the highest range in estimated temperature, 14ºC.

The disparity in $\delta^{18}O$ between samples from similar latitudes and age make global interpretation of these data challenging. However, comparing our data with output from an atmosphere general circulation model (AGCM) reveal a significant relationship between precipitation-minus-evaporation (P-E) and $\delta^{18}O_w$ estimated from $\delta^{18}O_{calcite}$. These results demonstrate the importance of interpreting $\delta^{18}O$ data in the context of global circulation patterns, ultimately showing that low $\delta^{18}O$ values in high latitudes specimens reflect runoff from ^{18}O-depleted seawater, rather than indicating lower global seawater $\delta^{18}O$ values.

ACKNOWLEDGEMENTS

I would like to thank my committee chair, Ethan Grossman, for his steadfast support and irreplaceable mentorship. I also appreciate my committee members, Juan Carlos Laya, Thomas Yancey, and Brendan Roark, for helping to guide me and supporting my research. I acknowledge and thank Chris Maupin for his academic and technical expertise and guidance, as well as his support in my time at SIGF.

Lastly, I would like to thank my family and friends, especially my parents Steve and Suzanne DePugh, for their unwavering love and support.

CONTRIBUTORS AND FUNDING SOURCES

Contributors

This work was supervised by a thesis committee consisting of Professor Ethan L. Grossman (advisor), Thomas Yancey, and Juan Carlos Laya of the Department of Geology and Geophysics and Professor Brendan Roark of the Department of Oceanography.

The data analyzed for this project were completed by Chris Maupin and student workers of the SIGF laboratory at Texas A&M University.

All other work conducted for the thesis was completed by the student independently.

Funding Sources

This research was supported by funds from the Michel T. Halbouty Chair in Geology.

TABLE OF CONTENTS

Page

LIST OF FIGURES

Page

LIST OF TABLES

Page

1. INTRODUCTION

The Permo-Carboniferous glaciation is one of four major periods of glaciation that occurred in the last billion years (Hyde et al., 1999). It not only represents the last time the Earth's climate fully transitioned from an icehouse climate to greenhouse climate (Fielding et al., 2008; Montanez et al., 2007), but it is also the only complete climate transition to have occurred on a vegetated Earth (Montanez et al., 2007). Studies of past climate change help us to understand the complex issues surrounding global temperature changes and its drivers as today's climate warms. The purpose of this study is to produce high-resolution snapshots of the seasonal ranges in the temperatures and salinities of mid-to-high latitude climates during the early Permian, a time of glacial retreat. To do so we generated $\delta^{18}O$ data from brachiopod shells sequentially-sampled along growth bands to produce an isotopic record that corresponds to the annual growth cycle of the specimen. These seasonal records characterize local seawater temperature and chemistry, which was then used to yield the mean annual range in temperature (MART) experienced by the brachiopod during its lifetime, providing an in-depth peek at climates past. To try to characterize the isotopic composition of seawater and climate, this study uses brachiopods from South America, Arctic Canada, Spitsbergen, and Western Australia. In doing so we try to gain a wider understanding of Permian seasonality in the Late Paleozoic.

1.1. Seasonality and Glaciation

Earth's seasonal cycle is dependent on the Earth's insolation and tilt, which is controlled by the orbital parameters: eccentricity, obliquity, and procession (Berger, 1978; Ashkenazy et al., 2010). These parameters vary on timescales from 20 kyr to 400 kyr and control MARTs, which increase with hotter summers and colder winters, and decrease with mild summers and winters. Over time, the slowly changing insolation will cause seasonal temperature ranges to grow or decline, causing either milder or more extreme seasons (Zachos et al., 2001). This is important because these seasonal temperatures contribute to ice volumes and global climate. Ice sheets form and expand at high latitude after years with consistently milder summers. This relationship was demonstrated by isotopic study of deep sea cores from the Cenozoic (Hays et al., 1976; Zachos et al., 2001) which showed that during milder boreal summers, less ice sheets were destroyed due to a decrease in summer insolation.

While orbital parameters are influential in the Earth's changing climate, they are not solely in control. Another important driver that contributes to glacial expansion and climate change is the carbon cycle (Zachos et al., 2001; Montañez and Poulsen, 2013). Lower atmospheric pCO_2 promotes cooling, while higher pCO_2 promotes warming, as in today's climate. These same factors that influenced ice sheet expansion in the Cenozoic were operating in the Permo-Carboniferous (Montañez and Poulsen, 2013). Other factors, such as topography, land mass distribution, and ocean circulation, are known to contribute to local glaciation and climate as well.

1.2. Late Paleozoic Climate

The Late Paleozoic Ice Age (LPIA) was originally believed to have occurred as a singular 70-Ma glacial event during the Permo-Carboniferous (Crowley and Baum, 1992), but most recent studies reveal that the LPIA occurred as a series of short-lived glacial events separated by contracted or ice-free climates (Hyde et al., 1999; Fielding et al., 2008; Montañez and Poulsen, 2013). Early modeling demonstrated one single, expansive ice sheet in the Southern Hemisphere while much of the lithologic, eustatic sea-level, atmospheric CO_2, and paleofloral data imply the LPIA was dynamic with episodic glaciations that expanded and contracted and eventually spread to the Northern Hemisphere (Montañez et al., 2007; Fielding et al., 2008; Montañez and Poulsen, 2013). Current reconstructions demonstrate that glaciation likely began with localized, short-lived, alpine glaciers, during the Latest Devonian and Early Mississippian (Fielding et al., 2008; Montañez and Poulsen, 2013). The onset of the LPIA is largely attributed to the assemblage and northern drift of Pangea (Hyde et al., 1999; Fielding et al., 2008), but a positive shift in marine $\delta^{13}C$ values indicates a drop in pCO_2 and models of Late Paleozoic orbital parameters suggest that there were multiple drivers influencing the dynamic ice volumes (Mii et al., 1999; Saltzman, 2002; Horton et al., 2012; Montañez and Poulsen, 2013).

These ice volumes grew from the latest Mississippian into the Pennsylvanian, where ice sheets expanded across South America, southern Africa, Australia, Oman, and Arabia. After a possible decrease in ice volumes in the mid to late Pennsylvanian, a massive expansion of ice sheets occurred at the Pennsylvanian – Permian boundary

(Fielding et al., 2008). Ice volumes peaked during the Asselian and early Sakmarian when glaciation became bipolar but declined thereafter. While some records have varying deglaciation rates, most agree that widespread and bipolar glaciation ended in the mid Permian (Fielding et al., 2008; Grossman et al., 2008; Korte et al., 2008; Laya et al., 2013a; Laya et al., 2013b; Montañez and Poulsen, 2013).

Understanding the key drivers of the LPIA is crucial to understanding global climate change. Orbital and atmospheric conditions were important elements that contributed to the nucleation, expansion, and retreat of glacial ice that occurred in Pennsylvanian and Permian climates (Crowley and Baum, 1992; Horton et al., 2007; Montañez et al., 2007; Horton et al., 2012). Hays et al. (1976) demonstrated that the cyclicity found in Pleistocene ice volumes was directly related to the timing of the Earth's changing orbital parameters, and the same relationship has been demonstrated in the Late Paleozoic as well. Modeling the relationship between ice volumes, seasonal temperature, and summer insolation, Horton et al. (2007) found that volumes were expanding when Southern Hemisphere summers were cool, and glaciation retracted when summers were warm. Atmospheric pCO_2 was highly variable during this time, and, because this greenhouse gas forces climatic changes, the pCO_2 has an inverse relationship with ice volumes (Hyde et al., 1999; Montañez et al., 2007; Fielding et al., 2008; Horton et al., 2012; Laya et al., 2013a).

1.3. Stable Isotope Paleothermometry and the LPIA

Stable isotope paleothermometry capitalizes on the relationship between $\delta^{18}O$ values of carbonate or phosphate minerals, and seawater temperature, but requires a

knowledge of the $\delta^{18}O$ of seawater ($\delta^{18}O_w$). The relationship between these three properties can be seen in the equation for calcite: T (°C) = 15.7 - 4.36 ($\delta^{18}O_{calcite}$ - $\delta^{18}O_w$) + 0.12 ($\delta^{18}O_{calcite}$ - $\delta 18O_w$)^2 (Hays and Grossman, 1991; O'Neil et al., 1969), where $\delta^{18}O_{calcite}$ is versus VPDB and $\delta^{18}O_w$ is versus VSMOW. When unknown, the $\delta^{18}O$ of the seawater is typically estimated based on the inferred ice volume at that time (e.g., Lear et al., 2000), but there are many environmental factors that can influence this value. For example, in environments where a significant component of surface waters is freshwater from large river input or glacial meltwaters, a carbonate's $\delta^{18}O$ value will be meaningfully influenced by the freshwater's isotopic values, usually resulting in a lower calcite $\delta^{18}O$ that, if undetected, would be misinterpreted as higher temperatures. Latitudinal variation in precipitation and evaporation will also influence $\delta^{18}O_w$ values (Zachos et al., 1994). Because of these factors, careful consideration is imperative when assuming a representative $\delta^{18}O_w$ for paleotemperature calculations (Grossman, 2012).

The Permo-Carboniferous isotopic record shows cooling in the early Permian. The glacial acme suggested by lithologic records occurred in the earliest Permian, during the Asselian or Sakmarian, and was followed by the subsequent stepping-down decrease in ice volumes until the Mid-Permian (Fielding et al., 2008; Laya et al., 2013a; Montañez and Poulsen, 2013). But, while isotopic records of the Permian confirm a similar acme as the lithologic records, they also challenge the conventional understanding of the subsequent warming. One notable oxygen isotopic record derived from brachiopods is presented in Korte et al. (2008). This record indicates a rapid ~2.5‰ decrease in $\delta^{18}O$ (warming) beginning in the latest Asselian and concluding in the

Artinskian. Conversely, the oxygen isotope record derived from conodonts shows a vastly different trend during the Permian (Chen et al., 2013). This record indicates a much longer glacial period, suggesting that ice volumes were stable in the Early Permian and first waned from the Kungurian to the Capitanian, when $\delta^{18}O$ decreased by ~2‰, while the isotopic record derived from brachiopods indicates a second phase of cooling beginning in the Artinskian and lasting until the Kungurian. This brachiopod record shows a warming trend for the remainder of the Permian with one minor episode of cooling in the Capitanian. The conodont record, on the other hand, displays large fluctuations in $\delta^{18}O$ at the Guadalupian-Lopingian transition, followed by a significant rise in $\delta^{18}O$ during the Lopingian and a rapid 3‰ decrease at the Permian-Triassic boundary (Chen et al., 2013).

The considerable differences found in these records can be attributed to regional environmental factors such as aridity, fresh water input, and evaporation. For example, the rapid $\delta^{18}O$ changes in the conodont record at the Guadalupian-Lopingian and P-T boundaries are simultaneous with episodes of volcanism (Chen et al., 2013). The variations may also be attributed to brachiopod diagenesis, because while low-Mg calcite is resistant to diagenesis, it is still susceptible to alteration. Biogenetic phosphate in conodonts is not nearly as vulnerable to fresh water diagenesis due to the strength of the phosphorus-oxygen bond and dense crystalline structure of these tooth-like microfossils (Pucéat et al., 2004). The conodont's preservation potential is why conodont isotopes are useful geochemical proxies for understanding ancient ocean chemistry.

1.4. LPIA Seasonality and Stable Isotope Paleothermometry

Seasonal climate studies of the Late Paleozoic have been conducted using stable isotope data from shell powders collected parallel to growth banding found in late Paleozoic carbonate specimens. Sampling in a grid-like pattern in cross-section, Mii and Grossman (1994) demonstrated that it is possible for ancient brachiopods to retain their original isotopic signatures, and that growth banding is identifiable in brachiopods by characteristic $\delta^{18}O$ variation across the shell. Using $\delta^{18}O$ values from 112 points sampled in a grid-like pattern across the billet of the specimen, and trace element analyses of 369 spots on the corresponding thin-section, the authors observed a 1½ to 2 year $\delta^{18}O$ cycle, which was the first Paleozoic seasonal record derived from oxygen isotopes. This study showed seasonal variation of 5 to 6°C (assuming $\delta^{18}O$ variations were due solely to temperature) in the late Pennsylvanian tropics and demonstrated that concentrations of the trace elements Mg, Na, and S increase with increasing temperatures.

Roark et al. (2016) studied low-latitude seasonality during a late Carboniferous highstand to understand the role of monsoonal circulation in controlling freshwater input into the Appalachian Basin of North America. Seasonal $\delta^{18}O$ records were produced from well-preserved brachiopods microdrilled along tracks parallel to growth banding. These records revealed a climate that was moist and relatively unvaried during this interglacial period. The authors concluded that this was due to a non-seasonal to weakly seasonal climate during the interglacial highstand, opposing climate simulations which indicated arid or strongly monsoonal tropical environments (Kutzbach and Gallimore,

1989). Roark et al. gave a high-resolution look into tropical climates during interglacial periods.

Ivany and Runnegar (2010) studied high-latitude seasonality in the Early Permian using $\delta^{18}O$ fluctuations along the growth axis of a well-preserved specimen of the bivalve *Eurydesma cordatum*. Seventy growth-band-parallel samples revealed six seasonal $\delta^{18}O$ cycles, yielding the "oldest multiannual record of primary isotope variation". The authors reported a nearly 12°C mean annual seasonal change, from 0 to 12°C, assuming a constant $\delta^{18}O_w$ value of -4‰. Although -4‰ is very low relative to modern seas (0‰), Ivany and Runnegar defended the value relating it to an expected meridional gradient and ultimately suggested that Paleozoic oceans were depleted in ^{18}O relative to modern oceans. These low seawater $\delta^{18}O$ values may be better explained by local environmental factors, such as the influence of freshwater via runoff or precipitation. Similar to these studies, the present study produces high-resolution seasonal records and provides detailed insights into the changing climates of the LPIA. In doing so, this study enhances the depth of understanding of mid- to high-latitude seasonality during the LPIA.

2. SAMPLES AND METHODS

2.1. Samples

Ideal specimens for this study are large, thick-shelled brachiopods from Late Paleozoic basins. Brachiopods produce shells of low-Mg calcite that are resistant to diagenesis, and had a widespread geographic distribution during the Paleozoic (Grossman et al., 2008). Another important criterion is that the brachiopods were deposited in mid-to-high latitude basins, as there is less seasonal variation in low latitudes, and ice volumes were predominate in the polar regions of the time. Also, brachiopods are preferred because they tend to precipitate shells near or at oxygen isotopic equilibrium with the ambient waters, minimizing vital effects (Grossman, 2012; but see later discussion).

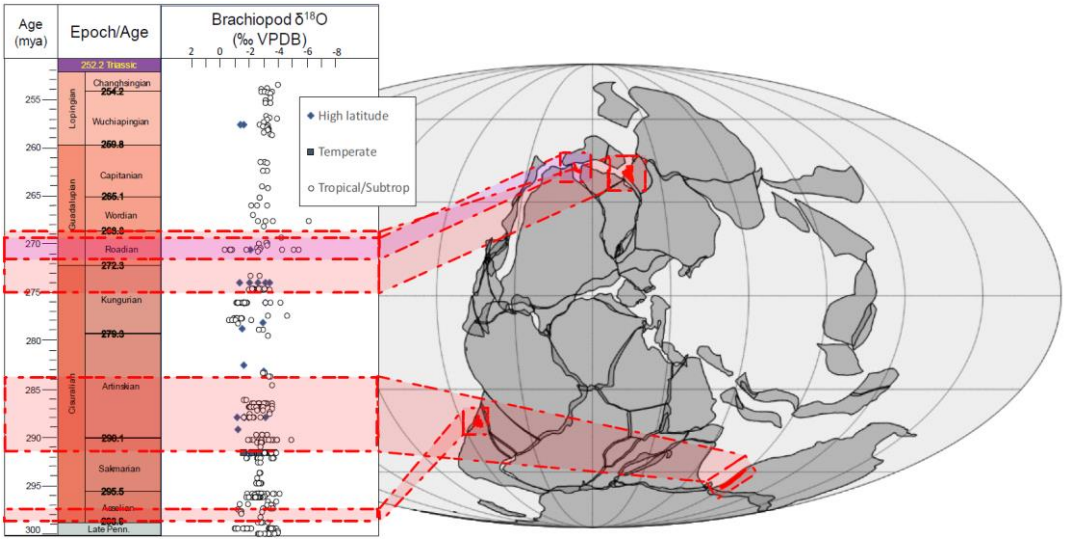

Figure 1 Sample locations, geologic time scale, and oxygen isotopic record. Isotope records from Grossman and Joachimski's recent work (submitted, GTS 2020).

Table 1: Sample information. Includes sample ID, age, taxon, lithology, environment of deposition (EOD), modern location, and paleo-latitude.

Sample	Age	Stage	Taxon	Lithology	EOD	Location	Paleolat, Paleolon
Spitsbergen, Kapp Starostin Fm.							
J001	268.8	Roadian	*Spiriferella polaris*	Consists of cherts and carbonates associated with fine-grained terrigenous sediments	Shells J001, J009, WSP 370, and WSA 586 represent a nearshore, shallow water marine bank facies. Shell WST 146 represents an open sea facies.	Polakkfjellet, Spitsbergen	45°N, 17°E
J009	270.15		*Spiriferella polaris*			Ahlstrandodden, Spitsbergen	
WST 146	267.12		*Spiriferella polaris*			Treskelodden, Spitsbergen	
WSP 370	270.15		*Spiriferella polaris*			Polakkfjellet, Spitsbergen	
WSA 586	270.15		*Cleiothyridina*			Ahlstrandodden, Spitsbergen	
Arctic Canada, Assistance Formation							
DI 6	270	Roadian	*Spiriferella sp*	Fine yellow to gray fossiliferous sandstone	Shallow inner ramp; water depth (~15-30 m)	Grinnell Peninsula, Devon Island, Canada	40°N, 0°
DI 9	270		*Neospirifer sp*				
Western Australia, Perth Basin, Holmwood Shale fm., Fossil Cliff Member							
PB4	285	Sakmarian-Artinskian	*Spirelytha fredericksi*	Interbedded micaceous and gypsiferous siltstone, sandy siltstone, and bioclastic calcarenite	Chiefly cold-water, low-energy marine depositional environments with fossiliferous limestone lenses representing shallow marine banks; water depth (~15-30 m)	Northern Perth Basin, Australia	60°S, 95°E
Western Australia, Carnarvon Basin, Callytharra Fm.							
CB 4	285	Sakmarian-Artinskian	*Imperiospira*	Mudstone and sandy mudstone with interbedded limestones marking the top of depositional cycles	Quiet, low energy period of deposition in a marine environment; water depth (~15-100 m)	Southern Carnarvon Basin, Australia	60°S, 110°E
CB 9	285		*Myodelthyrium*				
CB 14	285		*Elivina hoskingae*				
CB 16	285		*Myodelthyrium*				
Argentina, Del Salto Formation							
ADS 12	296	Asselian	*Pericospira sanjuanensis*	Alternating sandstone and mudstones with interbedded calcareous beds and lenses	Littoral to sub littoral marine deposits, depths unknown.	Del Salto Creek, Calingasta, San Juan, Argentina	50°S, 60°W

Shells used in this study are from four localities (Argentina, Australia, Devon Island, and Spitsbergen) from the Asselian, Sakmarian to Artinskian, Rodian, and Kungarian to Rodian (Figure 1, Table 1). The oldest specimen in this study is an Argentinian brachiopod from the Asselian Del Salto Formation. The *Pericospira*

sanjuanensis brachiopod is primarily found in the lower part of the Del Salto Formation, which is comprised of alternating sandstones and mudstones with intercalated calcareous beds and lenses (Figure 2). This section of the Del Salto Formation is interpreted to be a littoral to sub-littoral marine depositional environment from the latest Carboniferous into the early Permian (Cisterna and Archbold, 2007).

Figure 2 Sample location for Del Salto formation sample in modern Argentina. Location with stratigraphy of fossiliferous section of the Del Salto Formation. Figure reprinted from Cisterna and Archbold, 2007.

Samples from Western Australia are from the Sakmarian to Artinskian aged Fossil Cliff member of the Holmwood Shale formation in the northern Perth Basin and Callytharra Formation in the Carnarvon Basin (Figure 3). Both units are fully marine,

quartz-rich, limestones that were deposited in a progradational sequence (Haig et al., 2014). The taxa of the shells are *Imperiospira* sp., *Elivina hoskingae*, *Myodelthyrium* sp., and *Spirelytha fredericksi*.

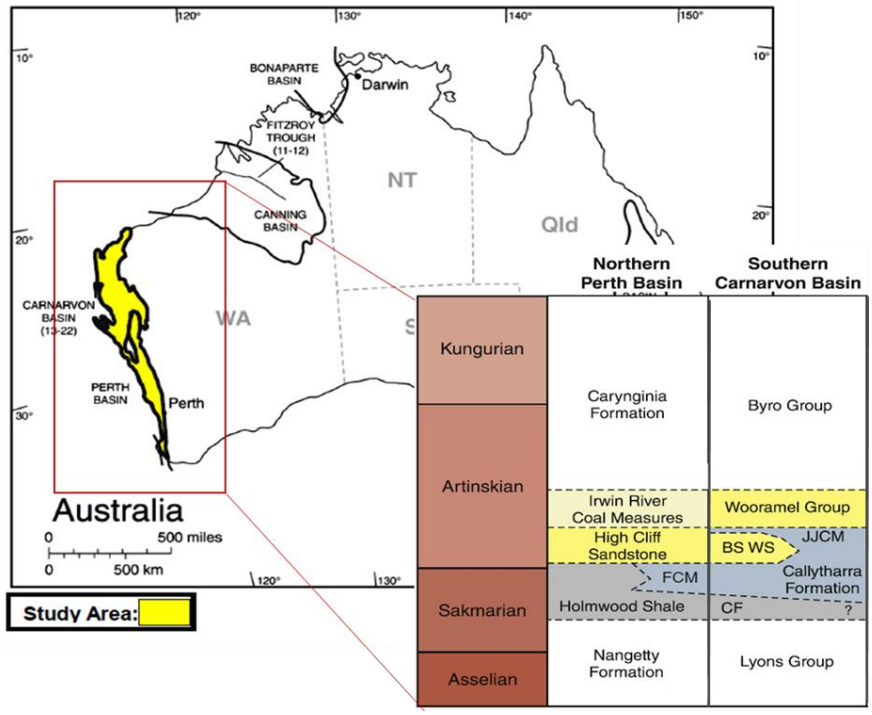

Figure 3 Sample location for brachiopods from Perth and Carnarvon Basins. Geographic location along with stratigraphy adapted from Haig et al., 2014.

The Spitsbergen shells are from the Kapp Starostin formation, which consists of limestone and chert deposits (Figure 4). The Kapp Starostin formation deposited during the Roadian (Kazanian) and Kungurian over multiple cycles of deposition. The deposits follow a transgressional sequence pattern changing upsection from nearshore to open marine deposits. The brachiopods in the formation are *Spiriferella polaris*, *Streptorhynchus kempii*, *Spiriferella hielhavii*, *Cleiothyridina* sp., *Svalbardoproductus* sp., and *Horridonia* sp. (Mii et al., 1997).

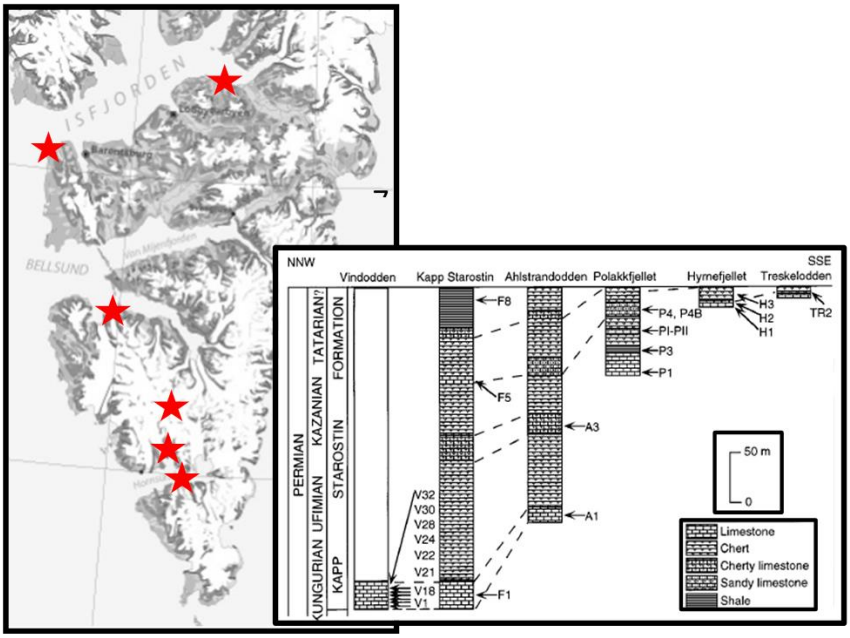

Figure 4 Sample locations for Kapp Starostin formation samples in modern Spitsbergen. Sampling locations and stratigraphy of the Kapp Starostin formation are adapted from Mii et al., 1997.

Brachiopods from Devon Island, Canada, are from the Assistance Formation in the Sverdrup Basin, and are Roadian in age. Taxa include the *Arctitreta triangularis, Horridonia* sp., and *Neospirifer* sp. The Assistance formation is composed of a fossiliferous sandstone with minor siltstone and fossiliferous calcareous concretions (Fig. 5), and is interpreted as an inner ramp transgressive sequence (Reid et al., 2007).

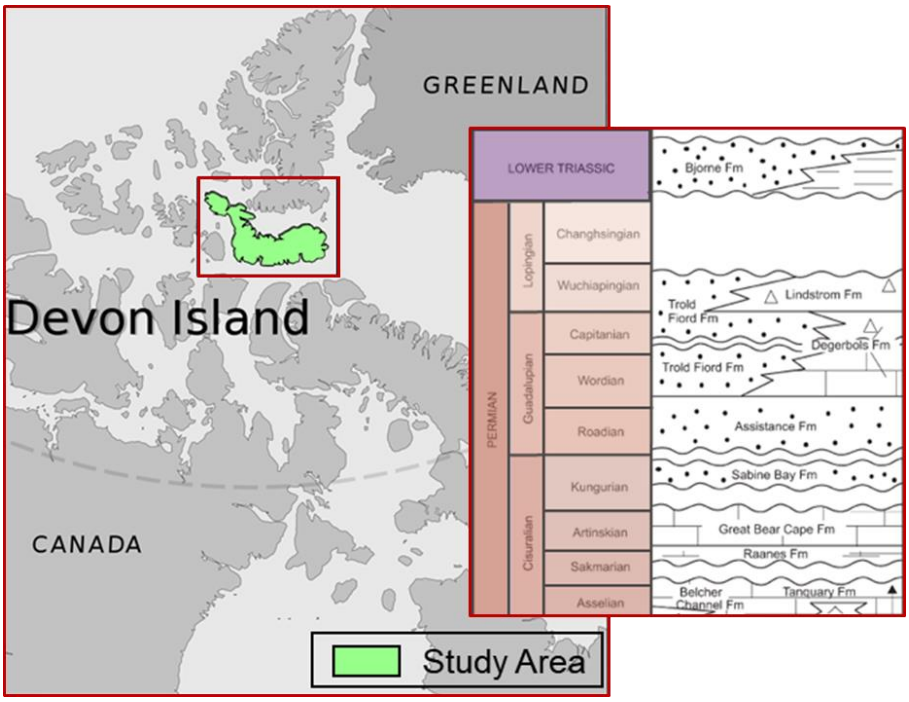

Figure 5 Sample location for Assistance formation samples in modern Devon Island, Canada. Devon Island study area and stratigraphy of the Assistance Formation are adapted from Reid et al., 2007.

2.2. Methods

Shells from Australia, Devon Island, and Spitsbergen were previously thin-sectioned (Mii and Grossman, 1997; Henkes et al., 2018), but the Argentinian specimen required thin-sectioning. We thoroughly cleaned the specimen of any dirt and encrusting materials using a toothbrush and then rinsed it in deionized water. Clean samples were dried and embedded in Struers Epofix epoxy. The epoxy was applied in layers to ensure that it would cure evenly, and each layer was cured for three days. The shell was then cut longitudinally using an Isomet saw. The billets were adhered to a frosted petrographic slide using Struers EpoFix epoxy and cured for an additional 3 days. The slides were trimmed to the appropriate size using a thin-sectioning saw, and polished using

gradationally finer grits. The finest grit used to polish was 0.3 μm deaglommerated alpha alumina. The thin-section was then examined for alteration under the stereo microscope for the presence of factures and secondary minerals, which would disrupt the primary crystal fabric. The thin-sectioned shells were stereoscopically examined in reflected and transmitted light for the presence of growth banding, and samples that lacked growth bands were excluded from further study.

All shells were then examined for diagenetic alteration under cathodoluminescence microscopy using a Technosyn 8200 MKII cold cathode luminoscope (Appendix I). The presence of Mn^{2+} in the crystal lattice is identified by orange luminescence in calcite after being exposed to a beam current of 200-300 nA and voltage of 10-15 KV. Mn^{2+} is considered to be a good indicator of diagenetic alteration when examining ancient brachiopod shells (Machel, 1985). Shells examined were photographed under plane light and cathodoluminescence and classified as nonluminescent (NL), slightly luminescent (SL), or cathodoluminescent (CL) (Flake, 2011). Fractures and matrix-filled voids typically were luminescent, providing a test for the effectiveness of the cathodoluminoscope. Shells classified as NL or SL were examined to identify nonluminescent well-preserved areas that were large enough for sampling. Shell areas classified as CL were not used in this study. Screening samples in this way helps reduce the scatter in the data and systematic error towards low values. High iron contents can quench luminescence but previous trace elemental analyses of these Spitsbergen shells (Mii et al., 1997) and *Elivina hoskingae* shells from the Callytharra formation (Western Australia; Mii et al., 2013) did not yield sufficiently high

iron contents for quenching. Thus we interpret nonluminescent shells to be well preserved.

Samples were obtained by collecting the powders from a series of parallel tracks drilled on a shell billet using a New Wave micromill with a 0.5 mm diameter drill bit. The tracks were 5000 μm x 100 μm with a depth of ~50 μm, and were oriented parallel to growth bands, along a transect perpendicular to growth bands (Figure 6). Sample powders of roughly 20-80 μg were loaded into a Kiel IV carbonate device, reacted in ~104% phosphoric acid, and the resulting CO_2 was analyzed on a Thermo Finnigan MAT 253 isotope ratio mass spectrometer in the Stable Isotope Geosciences Facility (SIGF) at Texas A&M University. Typical precisions are 0.03‰ for $\delta^{13}C$ and 0.07‰ for $\delta^{18}O$. Stable isotope data are standardized relative to the Cretaceous Peedee Belemnite (VPDB) using the reference material IAEA-603.

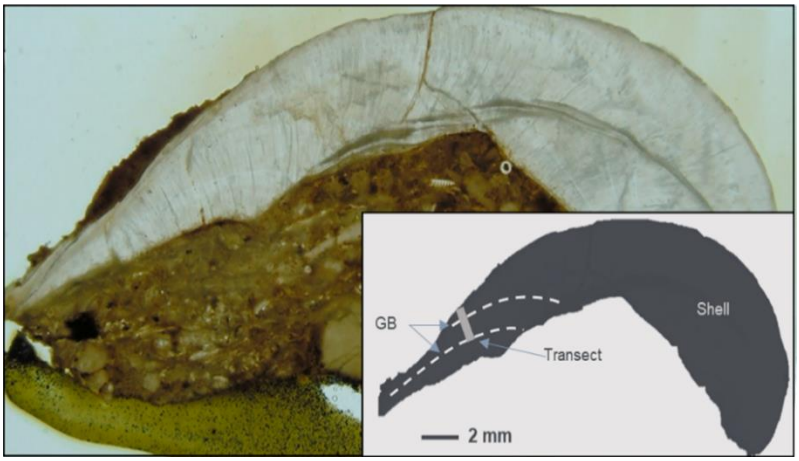

Figure 6 Photograph of brachiopod CB-14 thin-section with sample milling schematic. Sample is an *Elivina hoskinga* specimen from western Australia. Growth banding is outlined in a sketch of the shell using dotted lines and the sampling transect is indicated by a rectangle.

3. RESULTS

The isotopic records attained from each shell in this study, grouped by region, are shown in Figures 7-10, Table 2, and Appendix I and II. Figures 7 and 8 show the carbon and oxygen isotope records produced by the shells from the Southern Hemisphere. Our oldest record comes from the Argentinean shell, which is Asselian in age; its average $\delta^{18}O$ and $\delta^{13}C$ values are -4.9‰ and 4.3‰ respectively. The oxygen isotopic values range from -5.4 to -4.6‰, equivalent to a 4.5°C range in temperature, assuming constant $\delta^{18}O_w$. This record is quite distinct from the other Southern Hemisphere records in Figures 7 and 8, which are much higher in $\delta^{18}O$. These records that are derived from well preserved Sakmarian-to-Artinskian Australian brachiopods have an average $\delta^{18}O$ of -0.2‰ and an average $\delta^{13}C$ of 4.3‰. Most oxygen records (Figs. 7 and 8) exhibit regular variation around the average, the largest of which was CB 4, which shows a very negative $\delta^{18}O$ peak and large $\delta^{18}O$ range (2.1‰). This equates to a nearly 10°C change in temperature (assuming constant $\delta^{18}O_w$). The smallest variation found was in shell CB 16, with an oxygen isotopic range of 0.7‰, equivalent to approximately 3°C seasonality.

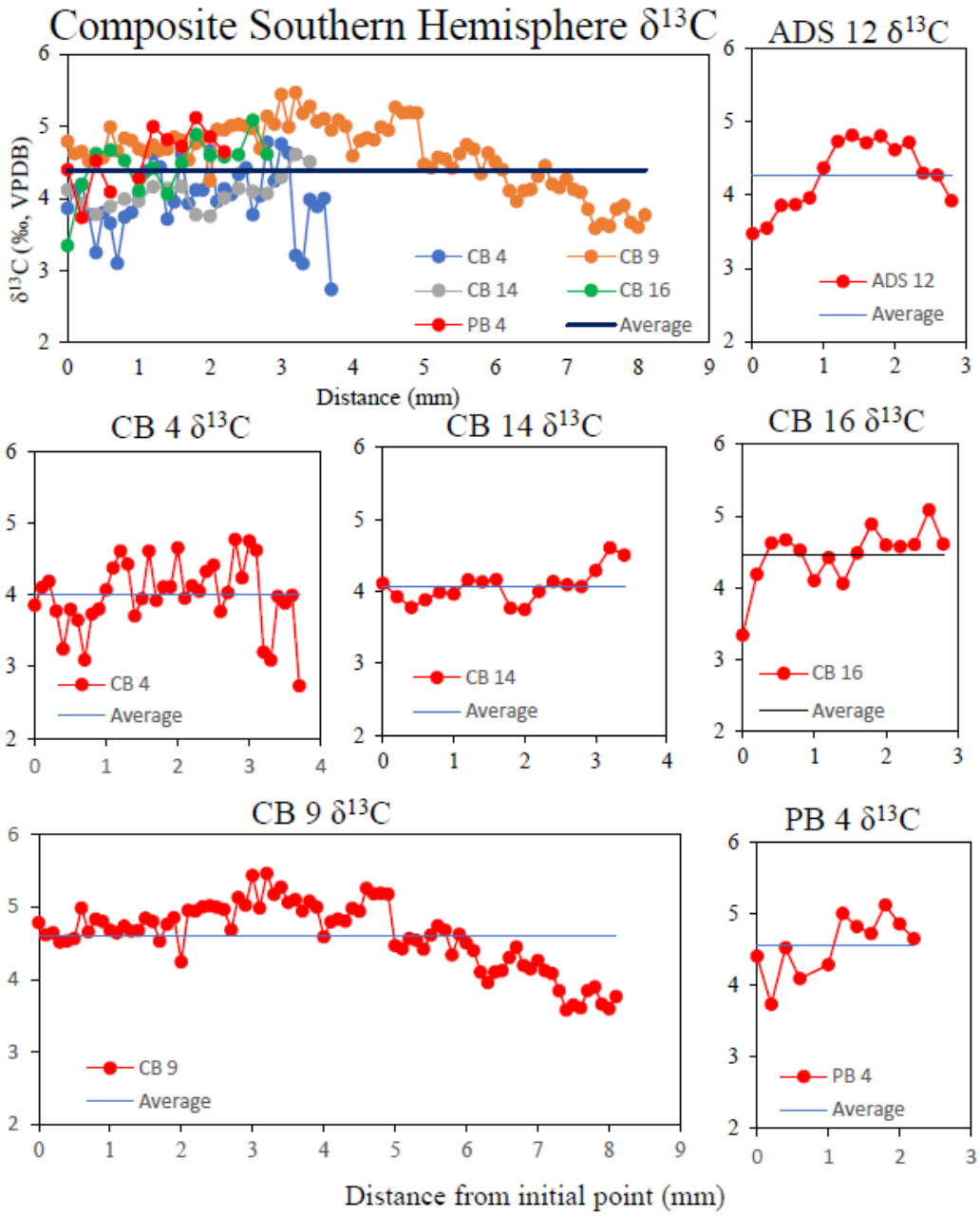

Figure 7- Southern Hemisphere $\delta^{13}C$ records. Carbon isotope records produced by the shells from the Southern Hemisphere. Horizontal axis is measured by millimeters from the initial analysis performed closest to the shell interior and moving across the shell toward the shell exterior. All shells from the Southern Hemisphere are represented in the composite, and their individual records are presented in red alongside the composite. Shells CB 4, CB 14, CB 16, and CB 9 are from the Carnarvon Basin, Shell PB 4 is from the Perth Basin, and Shell ADS 12 is from the Del Salto Formation.

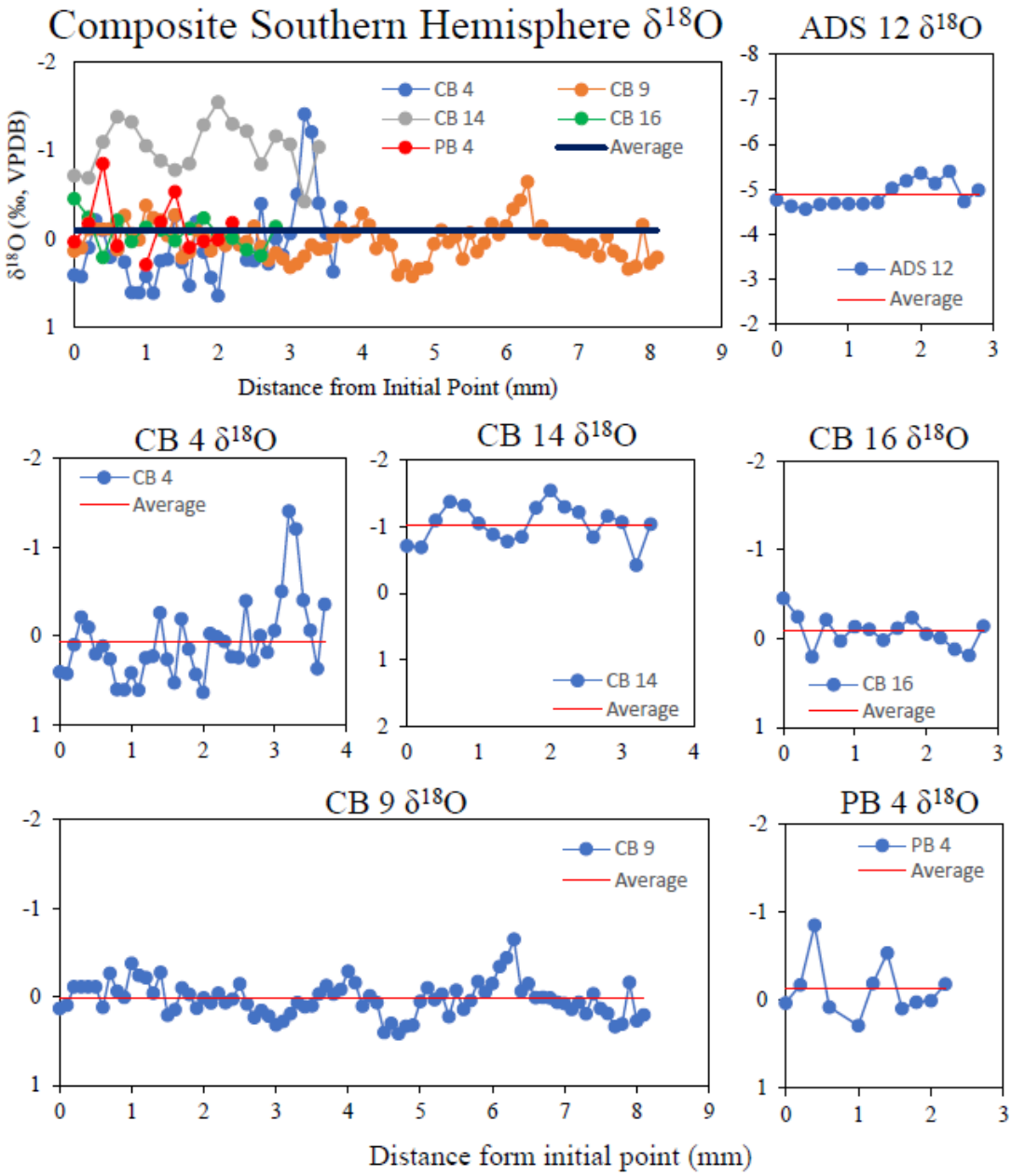

Figure 8- Southern Hemisphere $\delta^{18}O$ records. Oxygen isotope records produced by the shells from the Southern Hemisphere. Horizontal axis is measured by millimeters from the initial analysis performed closest to the shell interior and moving across the shell toward the shell exterior. All shells from the Southern Hemisphere are represented in the composite, and their individual records are presented in blue alongside the composite. Shells CB 4, CB 14, CB 16, and CB 9 are from the Carnarvon Basin, Shell PB 4 is from the Perth Basin, and Shell ADS 12 is from the Del Salto Formation.

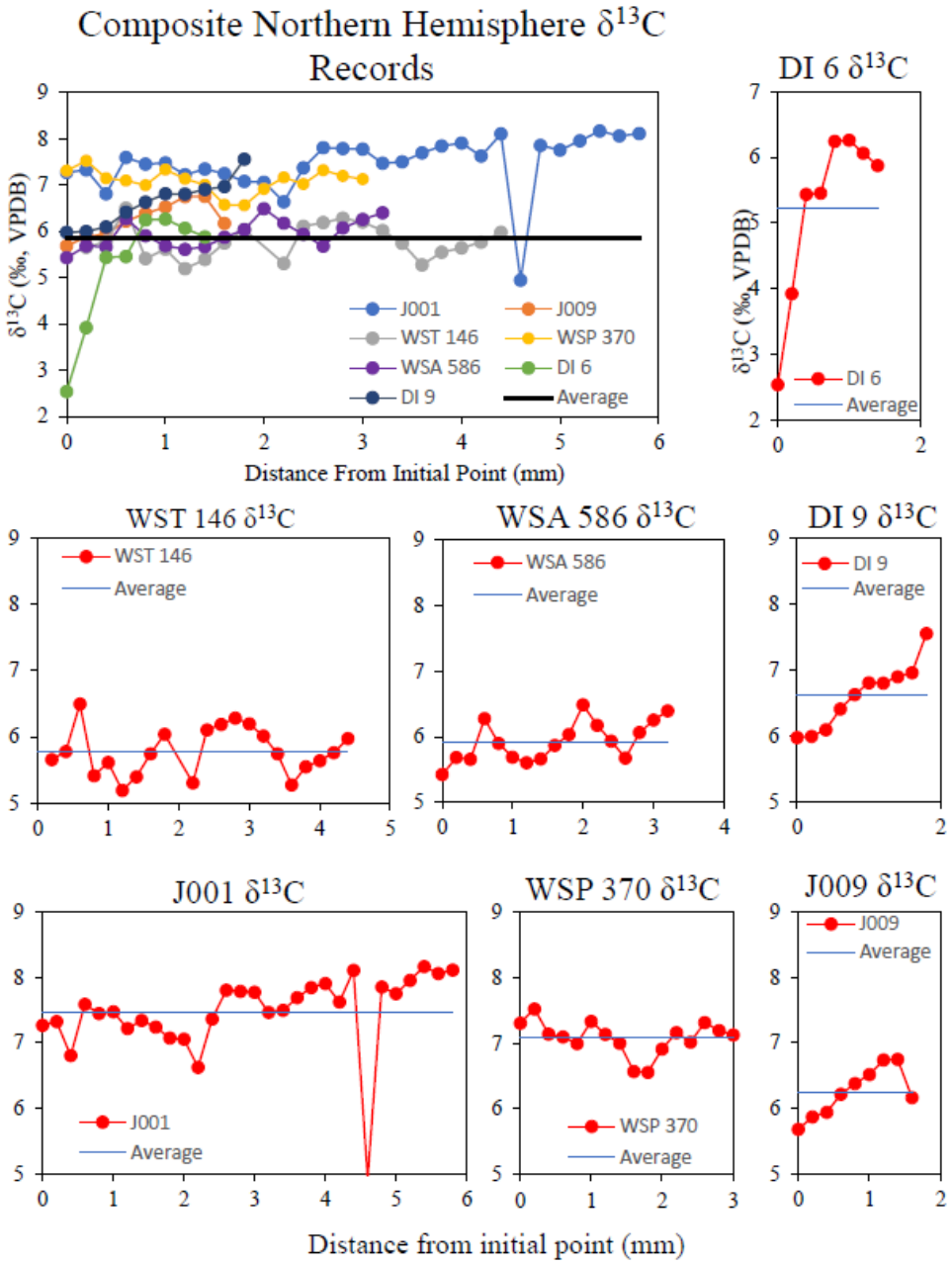

Figure 9- Northern Hemisphere $\delta^{13}C$ records. Carbon isotope records produced by the shells from the nothern hemisphere. Horizontal axis is measured by millimeters from the initial analysis performed closest to the shell interior and moving across the shell toward the shell exterior. All shells from the Northern Hemisphere are represented in the composite, and their individual records are presented in red alongside the composite. Shells DI 6 and DI 9 are from Devon Island, Canada and shells WST 146, WSA 586, J001, J009, and WPS 370 are from the Kapp Starostin Formation.

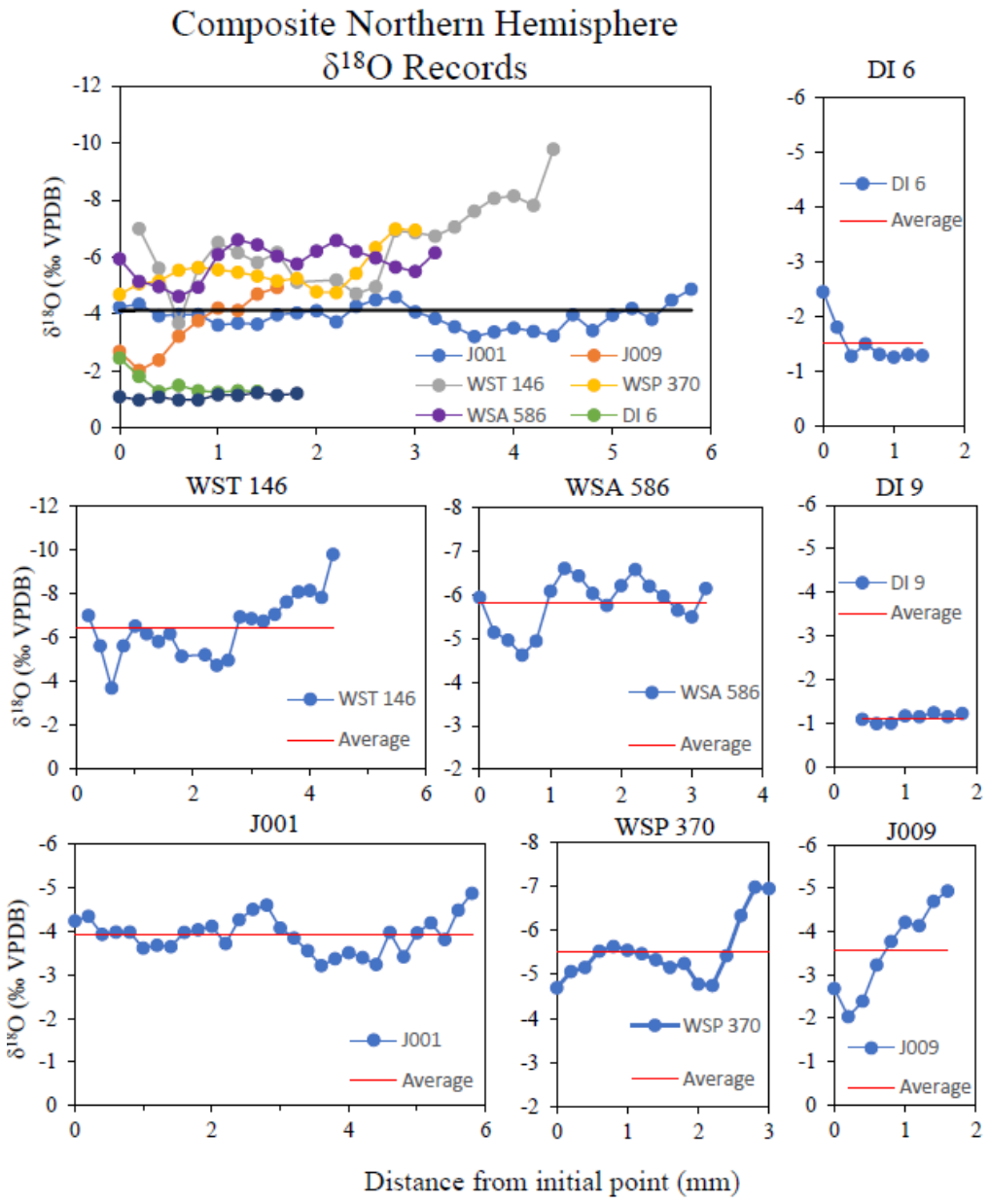

Figure 10- Northern Hemisphere $\delta^{18}O$ records. Oxygen isotope records produced by the shells from the Northern Hemisphere. Horizontal axis is measured by millimeters from the initial analysis performed closest to the shell interior and moving across the shell toward the shell exterior. All shells from the Northern Hemisphere are represented in the composite, and their individual records are presented in blue alongside the composite. Shells DI 6 and DI 9 are from Devon Island, Canada and shells WST 146, WSA 586, J001, J009, and WPS 370 are from the Kapp Starostin Formation

Figures 9 and 10 display the carbon and oxygen isotopic records of samples from Kungurian to Roadian brachiopods from Devon Island, Canada and Spitsbergen. Akin to the samples from Argentina, the $\delta^{18}O$ values from Spitsbergen are higher relative to those from Western Australia and Devon Island. The average $\delta^{18}O$ value for the Spitsbergen shells is -4.8‰, compared with -1.3‰ for Canadian shells. Seasonal variation is also present in the samples from Canada and Spitsbergen. The largest variation in $\delta^{18}O$ in this study is from a Spitsbergen shell (3.4‰), which, if $\delta^{18}O_w$ was constant, corresponds with an approximate 17°C range in temperature. Of the two Canadian brachiopods, the most $\delta^{18}O$ variation is from sample DI 6 (1.2‰), which is equal to a 6°C temperature range.

The carbon isotopes display variation as well, although this variation is neither consistent nor cyclical. ADS-12, the Argentinean brachiopod has an average $\delta^{13}C$ value of 4.3‰, with a max of 4.8‰ and min of 3.5‰. This gives a 1.3‰ range in $\delta^{13}C$ values, which is consistent with the average range in $\delta^{13}C$ at each location. The western Australian samples yield an average $\delta^{13}C$ of 4.6‰. The Northern Hemisphere locations display similar range averages, hovering around 1.85‰, but the average $\delta^{13}C$ values are higher, with the Canadian and Spitsbergen samples averaging 5.9‰ and 6.5‰, respectively. We attribute this higher value to variation in depositional environments and not seasonal signals. Figure 11 shows the scatter of $\delta^{13}C$ values versus $\delta^{18}O$ values for all shells used in this study; grouped by location using color, it illustrates the narrow range in $\delta^{13}C$ and $\delta^{18}O$ of these localities.

The isotopic values as well as the scale of isotopic variation seen in these high-resolution records are inconsistent spatially and temporally. Spitsbergen boasts the largest $\delta^{18}O$ seasonal variation and low $\delta^{18}O$ values, while time equivalent, latitudinally equivalent Canadian samples produce higher $\delta^{18}O$ values and much smaller $\delta^{18}O$ variation (Figure 12). We also see the lowest $\delta^{18}O$ values from our oldest (Asselian) and youngest (Roadian) specimen from distinct location, while the highest values are from the western Australian basins and are Sakmarian to Artinskian in age.

A study of the Spitsbergen shells by Mii et al. (1997) found that nonluminescent brachiopods in the Kapp Starostin formation returned average values for NL shell between -4.0 and -2.2‰ with minor exception. One exception is shell WST 146, which was found to yield $\delta^{18}O$ values of -7.2‰ and -3.5‰ in the Mii et al. (1997) study, and was found to have an average $\delta^{18}O$ value of -6.0‰ with a minimum $\delta^{18}O$ value of -7.1‰ and maximum of –3.7‰ in this study. While this shell was nonluminescent, a higher proportion of shells in the same and surrounding horizons were luminescent or slightly luminescent compared with the lower horizons in the formation. The records produced from this previous study are included with the data from this study in Table 4.

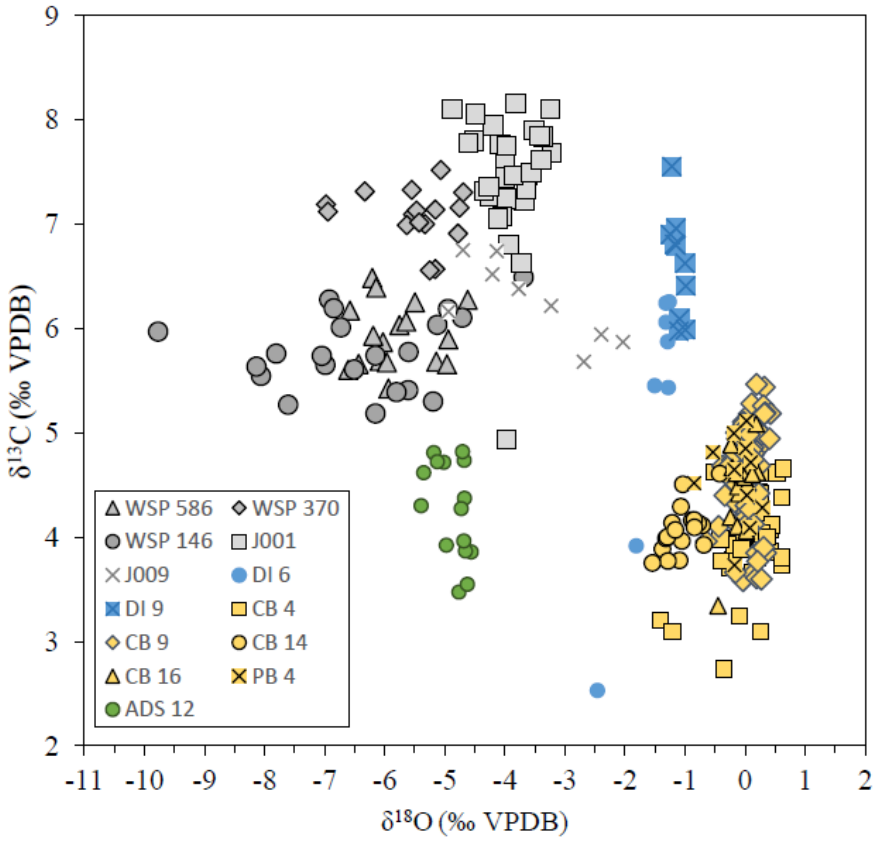

Figure 11- Scatter diagram of $\delta^{13}C$ vs $\delta^{18}O$ vales. Composed of all shells used in this study grouped by location using color, illustrating the narrow range in $\delta^{13}C$ and $\delta^{18}O$ of the localities. Gray symbols represent Spitsbergen brachiopods from the Kapp Starostin Formation, green symbols represent the shell from the Del Salto formation, in modern Argentina, yellow symbols represent shells from the Carnarvon and Perth Basins in modern western Australia, and blue symbols represent the shells from the Assistance formation of Devon Island, Canada.

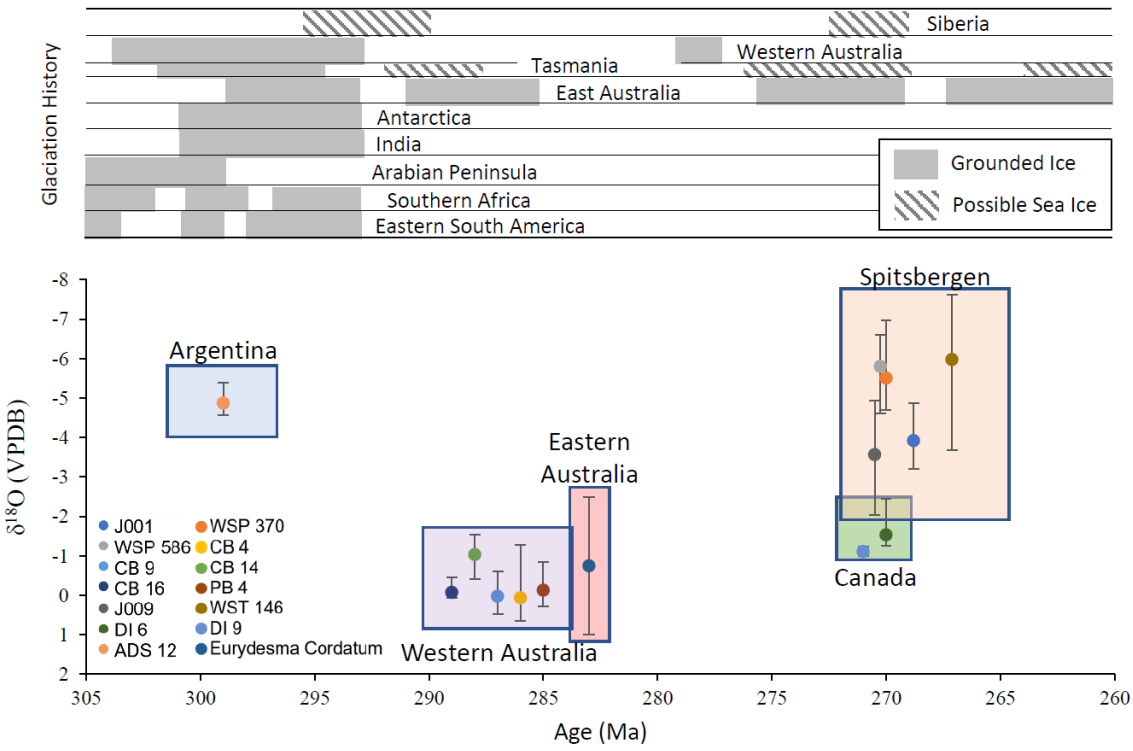

Figure 12- Comparison of glacial history and ranges in $\delta^{18}O$ versus age. Locations are indicated by colored boxes labelled by modern day location names. Samples from this study are labelled by Argentina, Western Australia, Spitsbergen, and Canada. Eastern Australia data are from Ivany and Runnegar (2010). Glacial history is adapted from Montañez and Poulsen (2013).

Table 2: Summary of CL character, average $\delta^{13}C$, and the average, maximum, minimum, and seasonal range in $\delta^{18}O$ of individual samples. Eastern Australia information from Ivany and Runnegar (2010). *Eurydesma cordatum* is from the Millfield Farm Formation near Cessnock, New South Wales, Australia and was deposited in shallow-water, volcanogenic sandstone containing an assemblage of brachiopods, bivalves, gastropods, and bryozoans at a paleolatitude of ~60°S.

Sample ID	*Taxa*	CL Character	*n*	$\delta^{13}C$ (‰, VPDB)	$\delta^{18}O$ (‰, VPDB)	$\delta^{18}O$ Max (‰, VPDB)	$\delta^{18}O$ Min (‰, VPDB)	Seasonal Range (‰, VPDB)
Spitsbergen, Kapp Starostin Fm.								
J001	*Spiriferella polaris*	NL	30	7.5	-3.9	-3.2	-4.9	1.67
J009	*Spiriferella polaris*	NL/SL	9	6.3	-3.2	-2.0	-4.2	2.2
WST 146	*Spiriferella polaris*	NL/SL	23	5.8	-5.9	-3.7	-7.1	3.4
WSP 370	*Spiriferella polaris*	NL	16	7.1	-5.2	-4.7	-5.6	1.0
WSA 586	*Cleiothyridina*	NL	17	5.9	-5.8	-4.6	-6.6	2.0
Average				**6.5**	**-4.8**	**-3.7**	**-5.7**	**2.0**
Arctic Canada, Assistance Formation								
DI 6	*Spiriferella sp.*	NL	8	5.2	-1.5	-1.2	-2.5	1.2
DI 9	*Neospirifer sp.*	NL	11	6.6	-1.1	-1.0	-1.2	0.3
Average				**5.9**	**-1.3**	**-1.1**	**-1.9**	**0.7**
Western Australia, Perth Basin, Holmwood Shale fm., Fossil Cliff Member								
CB 4	*Imperiospira sp.*	NL	38	4.0	0.1	0.6	-1.4	2.1
CB 9	*Myodelthyrium sp.*	NL	82	4.6	0.0	0.4	-0.7	1.1
CB 14	*Elivina hoskingae*	NL	18	4.1	-1.0	-0.4	-1.5	1.1
CB 16	*Myodelthyrium*	NL	15	4.5	-0.1	0.2	-0.5	0.7
Average				**4.3**	**-0.2**	**0.2**	**-1.0**	**1.2**
Western Australia, Canarvon Basin, Callytharra Fm.								
PB 4	*Spirelytha fredericksi*	NL	12	4.6	-0.1	0.3	-0.9	1.1
Average				**4.6**	**-0.1**	**0.3**	**-0.9**	**1.1**
Argentina, Del Salto Formation								
ADS 12	*Pericospira Sanjuanesis*	NL	15	4.23	-4.9	-4.6	-5.4	0.8
Average				**4.3**	**-4.9**	**-4.6**	**-5.4**	**0.8**
Eastern Australia, Ivany and Runnegar, 2010								
	Eurydesma Cordatum			**~5.5**	**~-0.75**	**1.0**	**-2.5**	**3.5**

4. DISCUSSION

Even though the intensity varies from shell to shell, regular, cyclical $\delta^{18}O$ variation is observed in shells from every location in this study, and, because these $\delta^{18}O$ variations closely correspond to the growth lines found in the shell's secondary layer, they are interpreted to reflect seasonal variation in the temperature and seawater $\delta^{18}O$ that occurred over the lifetime of the brachiopod. Some shell records, like those produced from J009 and DI 6, capture only one single annual cycle, while other records, such as CB 4 and CB 14, reflect multiannual paleoseasonality. Before examining the records in detail, however, we must first consider ^{18}O disequilibrium in brachiopod shells (i.e., vital effect).

4.1. Evaluation of Vital Effect

Brachiopods generally precipitate their shells at or near oxygen isotopic equilibrium with ambient seawater (Gonzalez and Lohmann, 1985; Grossman, 2012; Roark et al., 2017). However, this generality does have notable exceptions. Gonzalez and Lohmann (1985), Yamamoto et al. (2010), Auclair et al. (2003), and Romanin et al. (2018) illustrated lower $\delta^{18}O$ values indicative of disequilibrium fractionation in the outermost prismatic layer and, in some cases, the outer secondary layer of certain modern brachiopod taxa. Three shells in this study - WST 146, WSP 370, and J009 - show trends toward unusually low $\delta^{18}O$ values in nonluminescent interior layers close to the shell's exterior that likely reflect vital effects (Fig. 10; Appendix I). Close examination of these shells shows that sampling occurred across a change in shell

microstructure (Appendix I; A-14, A-15, and A-16) from prismatic tertiary layer into fibrous secondary layer. In contrast, the tertiary layers of these shells have $\delta^{18}O$ values that are completely consistent with the other shells from the same areas. These data were used in paleoenvironmental interpretations, whereas data suggestive of vital effect were excluded.

4.2. Calculating Paleotemperatures

In order to accurately calculate paleotemperatures the oxygen isotopic composition of the seawater ($\delta^{18}O_w$) must be estimated. For the Argentinian brachiopod sample, which is approximately 299 Ma, the global $\delta^{18}O_w$ is estimated to be 0‰, the modern values, as the ice volume during the earliest Permian is known to be high (Fielding et al., 2008). For the Australian specimen in this study, global $\delta^{18}O_w$ is assumed to be -0.75‰, because ice volumes in the middle Permian are thought to be low but are still significant enough to influence the isotopic composition of seawater (Fielding et al., 2008; E. Grossman, 2019, personal communication). Because of sedimentary evidence for declining ice volumes, temperatures for Roadian brachiopods from the Northern Hemisphere were calculated using an estimated $\delta^{18}O_w$ of -1.2‰.

Using these approximations and the calcite paleotemperature equation of O'Neil et al. (1969; as modified by Hays and Grossman, 1991) to calculate paleotemperatures, we have produced various ranges in temperature for sample locations. The Argentinean shell has a 4.6ºC range in temperature (~43ºC to 38ºC). These temperatures are unreasonably warm given the global climate at the time of deposition, which will be addressed later. The calculated temperatures and ranges from the Australian and

Canadian shells are more reasonable, comparatively. The Australian shells average 14ºC with a ~5ºC range in temperature, with a maximum temperature of 17ºC and minimum temperature of 12ºC. The Devon Island samples yield an average 4ºC temperature range with an average high of 20ºC and low of 16ºC. Similar to the Argentinean shell record, the shells from Spitsbergen also produce higher than reasonable temperatures, with an average temperature of 34ºC, and range from a high of 40ºC to a low of 27ºC.

In regards to global temperatures, these results reveal no trend related to temperature change associated with early Permian deglaciation. We found no relationship between $\delta^{18}O$ and ice volume, nor changes in seasonality with the warming climate.

4.3. Calculating Paleo-$\delta^{18}O_w$

We can use a different approach, assigning temperatures based on general circulation models, to explore possible ranges in seawater $\delta^{18}O$ associated with ranges in $\delta^{18}O_{calcite}$. The Asselian aged Argentinian brachiopod, which has a paleolatitude around 45°S, is expected to have experienced cool-temperate climate conditions (Tabor and Poulsen, 2008) indicating that the shells developed in waters that ranged from 10°C to 15°C in temperature (Archbold and Shi, 1995). Using these temperatures and the mean, minimum, and maximum $\delta^{18}O$ values, and assuming temperature is a dominant control on $\delta^{18}O$, produced from the Argentinian shell yields a $\delta^{18}O_w$ value of -5.6‰ for summer, -5.5‰ for winter, and -5.6‰ corresponding to a mid-point temperature of 12.5°C (Table 3). These $\delta^{18}O_w$ values are the lowest in this study.

While the low $\delta^{18}O$ values of the Argentina and Spitsbergen shells gave unreasonably warm paleotemperatures assuming $\delta^{18}O_w$ was 0‰ and -1.2‰ respectively, the Australian samples completely conform to expected temperatures and ranges. Faunal studies by Archbold and Shi (1995) indicate that the specimen from Australia likely experienced a temperate climate that averaged from 15°C to 20°C, which is exactly in-line with the temperatures found assuming a $\delta^{18}O_w$ of 0‰ (Table 2). Additionally, when calculating the $\delta^{18}O_w$ using Korte et al. (2008)'s expected temperature range and the average, low, and high $\delta^{18}O$ values produced from the Australian shells in this study, the $\delta^{18}O_w$ 0.1‰ using the coldest temperatures, 0.0‰ for the warmest temperatures, and 0.2‰ for the mid-point temperature of 17.5°C (Table 3).

Moving from Australia to Devon Island, we can assume the Canadian brachiopods formed in waters that ranged from 10-15°C, due to the presence of cool-water heterozoan faunas across the Sverdrup Basin during the Roadian (Reid et al., 2007). Using Reid et al. (2007)'s estimated temperature range and the $\delta^{18}O$ values of the Canadian shells yields a calculated $\delta^{18}O_w$ value of -2.1‰ for the summer, -2.5‰ for the winter, and -2.1‰ corresponding to the mid-point temperature (12.5°C, Table 3).

Lastly, the $\delta^{18}O_w$ value for the Spitsbergen samples was calculated using paleotemperature estimates from climate models (Crowley and Baum, 1992) and the average, low, and high $\delta^{18}O$ values produced from the Spitsbergen shells in this study. GCM simulations for a nearly ice-free, mid-latitude, Kazanian Spitsbergen indicate a temperature range from 15°C to 20°C yearly. Using this temperature range and brachiopod $\delta^{18}O$ values yields a calculated $\delta^{18}O_w$ value of -4.7‰ for summer, -3.9‰ for

winter, and -4.4‰ for the mid-point temperature of 17.5°C (Table 3). These values are also cause for concern, as they are far lower than expected for open marine conditions.

Table 3: Ranges in annual seasonal $\delta^{18}O_w$ derived from brachiopod $\delta^{18}O$ and AGCM-based temperatures. Temperatures are in ºC and $\delta^{18}O$ values are in ‰, VPDB.

			T based on AGCM			Measured			Estimated $\delta^{18}O_w$		
Location	**Age (mya)**	**Paleo Latitude**	**Summer T**	**Winter T**	**Average T**	**Summer $\delta^{18}O$**	**Winter $\delta^{18}O$**	**Average $\delta^{18}O$**	**Summer $\delta^{18}O_{sw}$**	**Winter $\delta^{18}O_{sw}$**	**Average $\delta^{18}O_{sw}$**
Spitsbergen	265-275	45	20	15	17.5	-5.7	-3.7	-4.8	-4.7	-3.9	-4.4
Arctic Canada	270	45	15	10	12.5	-1.9	-1.1	-1.3	-2.1	-2.5	-2.1
Western Australia	285	60-70	20	15	17.5	-1.0	0.2	-0.2	0.0	0.1	0.2
Argentina	299	45	15	10	12.5	-5.4	-4.6	-4.9	-5.6	-5.5	-5.6

4.4. Clumped Isotope Paleothermometry

Due to the complex relationship between the isotopic composition of seawater, temperature, and the isotopic value found in calcite shells, many isotope geochemists are investigating a new paleothermometer that does not rely on the value of the environmental $\delta^{18}O_w$. Clumped isotope thermometry is founded on the tendency for isotopically heavy carbon and oxygen atoms (^{13}C and ^{18}O) to preferentially pair within the calcite mineral lattice (Ghosh et al., 2006). This relationship can be expressed by:

$$Ca^{12}C^{16}O + Ca^{13}C^{18}O^{16}O \leftrightarrow Ca^{12}C^{18}O^{16}O + Ca^{13}C^{16}O$$

and can be used as a paleothermometer because the ion exchange is thermodynamically controlled (Ghosh et al., 2006). Clumped isotope thermometry defines the relationship between the fraction of $^{13}C^{18}O^{16}O_2^{2-}$ ions present in a carbonate mineral and the temperature of precipitation or reequilibration. The homogenous equilibrium, or solid-

state exchange, that occurs within the carbonate mineral's lattice denotes that there is no isotopic exchange outside of the mineral, and it is therefore not dependent on the environmental waters present when the mineral formed (Ghosh et al., 2006). This characteristic significantly separates clumped isotope thermometry from oxygen isotope thermometry and could help to better define ancient climates.

Fortunately, we have the opportunity to directly compare some of our stable isotope results to clumped isotope analyses that used the same shells. The Canadian and Australian shells used in this study were analyzed by Henkes et al. (2018). Interestingly, a similar Devon Island seawater $\delta^{18}O$ was derived in both studies, although the $\delta^{18}O_w$ average is slightly higher in this study (Table 4). The Henkes study finds a temperature of 10°C and 17°C for the two shells that were used in this study. These are completely reasonable temperatures, considering paleoclimate indicators categorized the Assistance Formation paleoclimate as cool-temperate (Reid et al., 2007).

While the clumped data seem to faithfully align to our own study for Canadian specimens, the Australian shells are a bit divergent. The $\delta^{18}O$ values are consistent with our own, but the derived temperatures, up to 33 ± 8°C, and the seawater $\delta^{18}O$ values, up to ~3.0‰, are higher than our estimates. While clumped isotopes can remove the guesswork in determining paleotemperature, the methodology is complex and the errors can be large.

4.5. Paleosalinity

Although brachiopods typically prefer normal marine salinities and are not commonly found in hypersaline or brackish waters (Fürsich and Hurst, 1980), the lower-

than-expected $\delta^{18}O_w$ values and corresponding salinities should be explored. Salinity trends are predominantly influenced by global trends in precipitation and evaporation, and are closely related to latitudinal variation, but local factors may also influence regional variation in seawater chemistry; for example, possibly restricted mixing with ^{18}O-depleted runoff from snowmelt and high-latitude precipitation may lower the regional salinity and seawater $\delta^{18}O$ (Mii et al., 1997; Grossman et al., 2008; Ivany and Runnegar, 2010). But while these influences alone would probably not be substantial enough to produce such low $\delta^{18}O$ values as were seen in Argentina and Spitsbergen brachiopods (Brand et al., 2003), comparing these data with output from an atmosphere general circulation model (AGCM) reveals a significant relationship between precipitation-minus-evaporation (P-E) and $\delta^{18}O_w$ estimated from $\delta^{18}O_{calcite}$.

Figure 13 shows salinity curves assuming mixing with ^{18}O-depleted waters with endmember fresh-water oxygen isotope values ($\delta^{18}O_{fw}$) of -10‰ and -15‰. These $\delta^{18}O_{fw}$ values were estimated considering latitude and geographic distribution of modern and modeled Paleogene values (Roberts et al., 2011). Salinities for areas with relatively high $\delta^{18}O_w$, such as Western Australia (0.2‰) and Arctic Canada (-2.1‰), had low variability and higher values. The Western Australian salinities ranged from 37 to 38 PSU, potentially indicating excess evaporation. Areas with low $\delta^{18}O_w$, like Spitsbergen (-4.6‰), yield a low salinity range from 21 to 26 PSU, indicating substantial freshwater input.

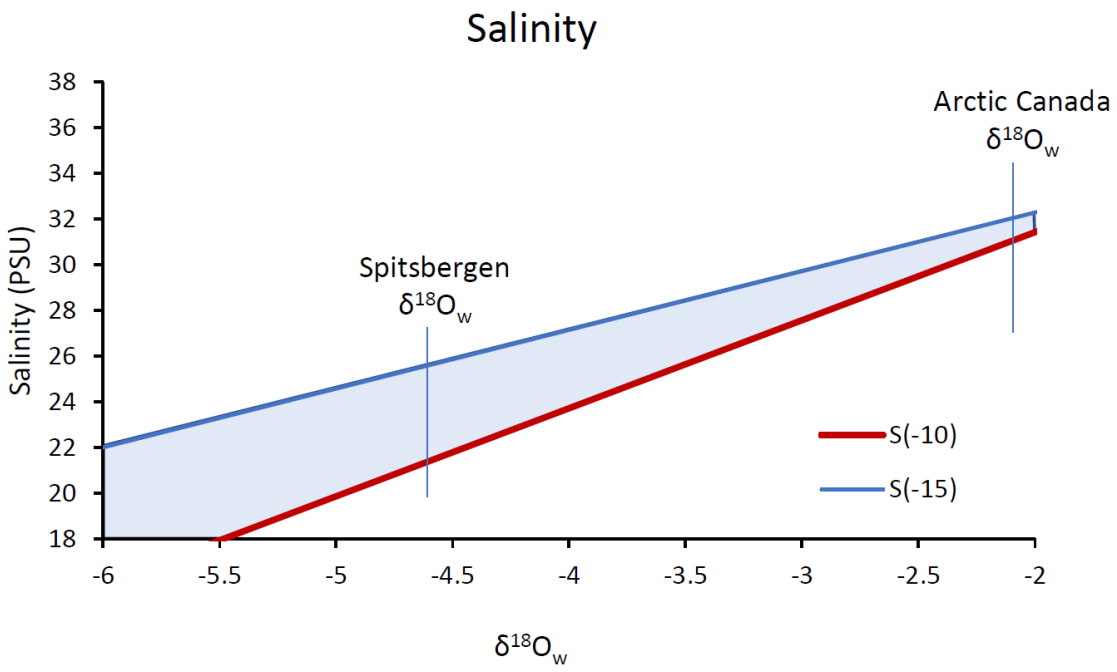

Figure 13- Salinity vs $\delta^{18}O_w$ curves. Curves used to estimate salinity range per derived $\delta^{18}O_w$. Endmember $\delta^{18}O_{fw}$ values, -10‰ and -15‰, were estimated based on latitude and geographic distribution of modern and model Paleogene $\delta^{18}O_{fw}$, while ocean salinity is assumed to range from 34.35 to 35 PSU. Lines representing the estimated Spitsbergen and Arctic Canada $\delta^{18}O_w$ are drawn across the salinity curves to show the estimated range in salinities at each location.

Figures 14 and 15 show P-E maps for 285 Ma and 270 Ma, respectively. These were produced by the Genesis 2 AGCM (Thompson and Pollard, 1997) and Genesis 3 AGCM (Richard et al., 2018) respectively. The model for the 285 Ma P-E map uses the paleogeography from Scotese et al. (1999) and a 50-m thick slab ocean, ocean heat flux modeled as linear diffusion, while the 270 Ma P-E map uses the Ziegler et al., (1997) paleogeography, and both reconstructions use pCO_2 = 4x pre-industrial atmospheric levels (Grossman et al., 2002; Richard et al., 2018; E. Grossman, 2019, pers. comm.). The study area that had the lowest brachiopod $\delta^{18}O$ values, present-day Argentina, is also

an area with excess precipitation. Argentina received a net precipitation rate from 3 to 5 mm/day annually and has an $\delta^{18}O_w$ value of -5.6‰ as an average. When considering the P-minus-E map for 270 Ma, the area with the lower $\delta^{18}O_w$ value is in an area that experiences more precipitation; Spitsbergen has a net precipitation rate up to 1 mm/day and has a $\delta^{18}O_w$ value of -4.6‰ on average. The Canadian samples have a lower net precipitation rate (0 to -1 mm/day) and higher $\delta^{18}O_w$ value, approximately -2.1‰. Perhaps most interestingly, the samples from the western coast of Australia yielded the highest $\delta^{18}O_w$ value, with an average of 0.2‰, while the eastern coast provided a low $\delta^{18}O_w$ value (-4‰; Ivany and Runnegar, 2010). This divergence between eastern and western Australian $\delta^{18}O_w$ values seems problematic given the proximity of the basins, but when they are considered alongside their respective precipitation rates, a potential explanation becomes clear. The Perth and Carnarvon basins are located on the western coast of Australia, which had a net precipitation rate of 1 to -1 mm/day. This is markedly unlike the high (2 to 3 mm/day) precipitation rate near modern-day Cessnock, Australia on the east coast. These data from these locations indicate a strong inverse relationship between AGCM-derived net precipitation and estimated $\delta^{18}O_w$ for the area. This relationship is also apparent for areas that are not adjacent, or even of the same latitude, but have similar a net precipitation. For example, in locations where the net precipitation is similar (i.e. Argentina (2 to 3 mm/day) and eastern Australia (2 to 3 mm/day)), we see similarly high $\delta^{18}O_w$ values (-5.6‰ and -4.0‰).

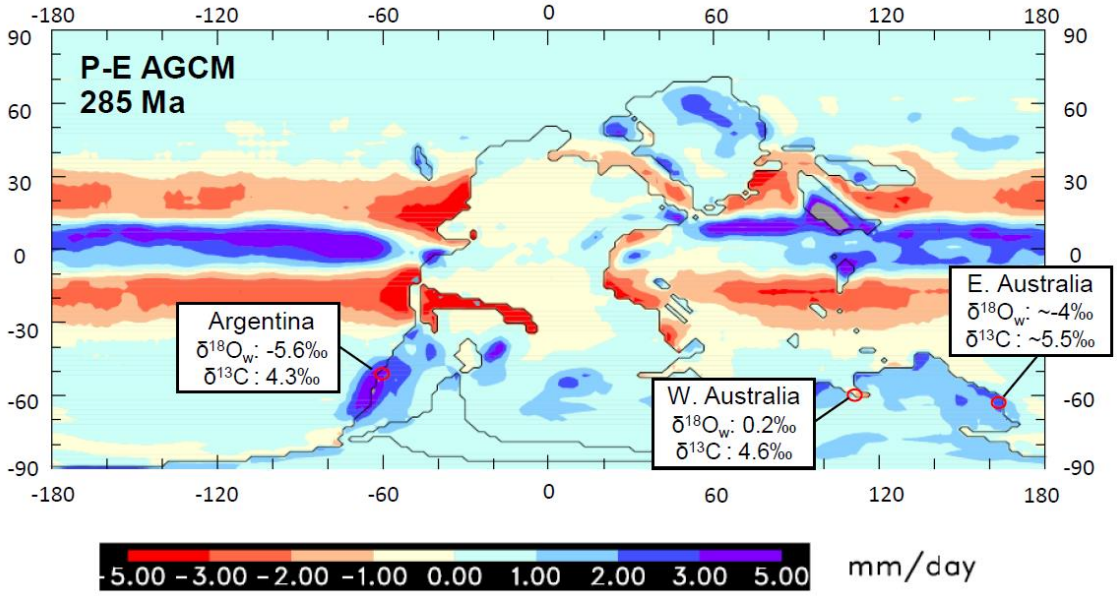

Figure 14- Precipitation-minus-evaporation map from atmosphere general circulation model (AGCM) for 285 Ma compared with estimated seawater $\delta^{18}O$ and measured brachiopod $\delta^{13}C$. Measured data is from shells in this study and Ivany and Runnegar (2010; E. Australia). Model (Genesis 2) uses paleogeography from Scotese et al. (1999), 50-m thick slab ocean, ocean heat flux modeled as linear diffusion, and pCO_2 = 4x pre-industrial modern (Grossman et al., 2002; E. Grossman, 2019, pers. comm.). See Pollard and Thompson (1997) for more details on the AGCM. Note that areas with excess precipitation correlate with areas of lower $\delta^{18}O_w$ values.

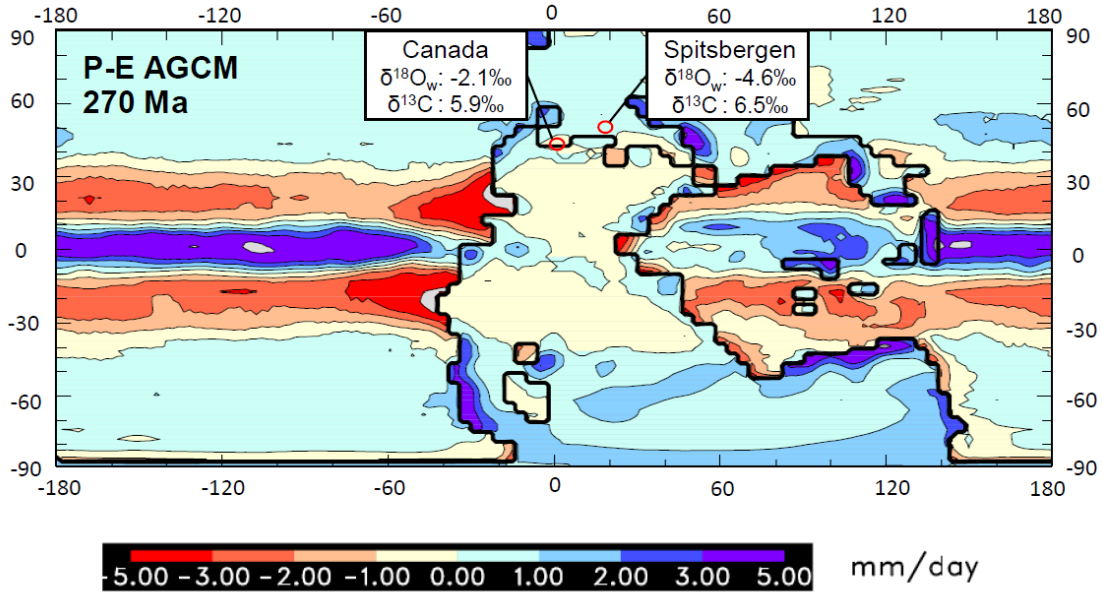

Figure 15- Precipitation-minus-evaporation map from atmospheric general circulation model (AGCM) for 270 Ma compared with estimated seawater $\delta^{18}O$ and measured brachiopod $\delta^{13}C$. Measured data is from this study's Canadian and Spitsbergen shells. Model (Genesis 3) is adapted from Ziegler et al. (1997) and uses a pCO_2 = 4x pre-industrial modern (Richard et al., 2018). See Pollard and Thompson (1997) for more details on the AGCM.

Waters with low salinity and $\delta^{18}O$ are expected to also have low $\delta^{13}C$ values for dissolved inorganic carbon (DIC), thus resulting in shells with low $\delta^{13}C$ and $\delta^{18}O$. In this study, the relationship between $\delta^{13}C$ and $\delta^{18}O_w$ is not consistent; however, the area with the lowest $\delta^{18}O_w$ value (Argentina) does correspond to the lowest $\delta^{13}C$.

These results demonstrate the importance of interpreting $\delta^{18}O$ data, especially those from restricted basins, in the context of global circulation patterns and paleo-precipitation. Thus low $\delta^{18}O$ values in high latitudes, rather than indicating lower global seawater $\delta^{18}O$ values, may reflect runoff from ^{18}O-depleted seawater.

Table 4: Compilation of isotopic values derived in this and previous studies. Data additional to this study are comprised of Eastern Australia data from Ivany and Runnegar (2010), Western Australia and Devon Island Canada values from Henkes et al. (2018), and Western Australia and Spitsbergen data from Mii et al. (1997, 2013).

Sample ID	$\delta^{18}O$ (‰, VPDB)	$\delta^{13}C$ (‰, VPDB)	T (°C)	Δ_{47}	Δ_{47}T (°C)	$\delta^{18}O_w$ (‰, VPDB)
Spitsbergen (this study)						
J001	-3.9	7.5	15-20	-	-	-3.5
J009	-3.6	6.3		-	-	-2.8
WST 146	-6.0	5.8		-	-	-5.5
WSP 370	-5.5	7.1		-	-	-4.8
WSA 586	-5.8	5.9		-	-	-5.4
Average	**-4.8**	**6.5**		-	-	**-4.4**
Spitsbergen (this study)						
DI 6	-1.5	5.2	10-15	-	-	-2.3
DI 9	-1.1	6.6		-	-	-1.9
Average	**-1.3**	**5.9**		-	-	**-2.1**
Western Australia (this study)						
CB 4	0.1	4	15-20	-	-	0.5
CB 9	0.0	4.6		-	-	0.4
CB 14	-1.0	4.1		-	-	-0.6
CB 16	-0.1	4.5		-	-	0.3
PB 4	-0.1	4.6		-	-	0.3
Average	**-0.2**	**4.3**		-	-	**0.2**
Argentina (this study)						
ADS 12	-4.9	4.3	10-15	-	-	-5.6
Average	**-4.9**	**4.3**		-	-	**-5.6**
Eastern Australia (Ivany and Runnegar, 2010)						
Eurydesma Cordatum	~-0.75	~5.5	0-12	-	-	**-4**
Western Australia (Henkes et al., 2018)						
CB 4	-0.01	4.11		0.677	33 ± 8	3
CB 9	-0.77	4.48		0.696	25 ± 12	1.1
CB 14	-0.38	3.98		0.699	24 ± 9	0.1
CB 16	-0.17	4.28		0.697	25 ± 16	1.2
PB 4	0.02	4.03		0.721	15 ± 7	-0.5
Average	**-0.262**	**4.176**		**0.698**	**24.4**	**0.98**
Western Australia, Callytharra Formation (Mii et al., 2013)						
Average	**-0.1± 0.5‰**	**4.4 ± 0.5‰**	2-7	-	-	-
Arctic Canada (Henkes et al., 2018)						
DI 6	-1.76	6.43		0.716	17 ± 7	-1.9
DI 9	-1.17	6.06		0.736	10 ± 7	-2.9
Average	**-1.465**	**6.245**		**0.726**	**13.5**	**-2.4**
Spitsbergen (Mii et al., 1997)						
J001	-3.9	8	15-20	-	-	-2.7
J009	-3.2	5.1		-	-	
WST 146	-5.35	6		-	-	
WSP 370	-4.5	7.6		-	-	
WSA 586	-5.95	5.7		-	-	
Average	-4.58	6.48		-	-	

5. CONCLUSIONS

We analyzed the $\delta^{18}O$ and $\delta^{13}C$ of Permian brachiopod shells to examine temporal and spatial trends in temperature and salinity in mid to high paleolatitudes during the transition from the Asselian glacial maximum to the Kungurian/Roadian glacial retreat. Data were collected from shells from Argentina, Australia, Canada, and Spitsbergen spanning from the Asselian to the Roadian. We found that the relationships between the oxygen isotope data were most naturally defined by location, with little evidence of a temporally defined relationship across our samples. This is reinforced by the fact that samples of the same age from Arctic Canada and Spitsbergen had very different $\delta^{18}O$ and $\delta^{13}C$ values.

The seasonal trends and mean isotopic compositions from each location were disparate. The Asselian-aged Argentinian brachiopod had consistently low $\delta^{18}O$ and $\delta^{13}C$ values. The seasonal variability in $\delta^{18}O$ was from -4.6‰ to -5.4‰, which corresponds to a 5ºC range in annual temperature assuming constant seawater $\delta^{18}O$. Western Australia brachiopods, which were Sakmarian to Artinskian in age and yielded the highest $\delta^{18}O$ values of the study, had a similar annual temperature range of 5ºC, but with drastically different $\delta^{18}O$ values (0.2‰ to -1.0‰). Arctic Canada shells yielded the smallest range in annual temperature, equivalent to 3ºC, and had moderately high $\delta^{18}O$ values and high $\delta^{13}C$ values. These Roadian shells from Canada were of the same age as the Spitsbergen brachiopod shells, but their records were much different. The Spitsbergen shells provided the lowest $\delta^{18}O$ values, the highest $\delta^{13}C$ values, the highest seasonal range in

$\delta^{18}O$ (from -3.65‰ to -6.2‰) and thus the highest range in estimated temperature, 14ºC. Both shell locations were in the Northern Hemisphere, at a similar latitude (~45º), and from approximately the same time, yet they yield contrasting records.

This $\delta^{18}O$ disparity between similar regions and times make relating these data to global climate change challenging. However, comparing our oxygen isotope data and those of Ivany and Runnegar (2010) with regional precipitation-minus-evaporation (P-E) patterns based on atmosphere general circulation models reveals a startling correlation between low $\delta^{18}O$ and high P-E. This demonstrates a strong relationship between paleosalinity and shell $\delta^{18}O$.

This study illustrates the importance of interpreting $\delta^{18}O$ data within the context of paleogeography and atmospheric and ocean circulation. When considered alone, data like those for Spitsbergen and Argentina brachiopods could have implied high temperatures or lower global seawater $\delta^{18}O$, but our study shows that lower $\delta^{18}O$ values are more likely the result of runoff from ^{18}O-depleted seawater.

REFERENCES

Archbold, N. W., and Shi, G. R., 1995, Permian brachiopod faunas of Western Australia: Gondwanan—Asian relationships and Permian climate: Journal of Southeast Asian Earth Sciences, v. 11, no. 3, p. 207-215.

Ashkenazy, Y., Eisenman, I., and Gildor, H., 2010, The Effect of Milankovitch Variations in Insolation on Equatorial Seasonality: Journal of Climate, v. 23, no. 23, p. 6133-6142.

Auclair, A.-C., Joachimski, M. M., and Lécuyer, C., 2003, Deciphering kinetic, metabolic and environmental controls on stable isotope fractionations between seawater and the shell of Terebratalia transversa (Brachiopoda): Chemical Geology, v. 202, no. 1-2, p. 59-78.

Berger, A., 1978, Long-Term Variations of Daily Insolation and Quaternary Climatic Changes: Journal of the Atmospheric Sciences, v. 35, no. 12, p. 2362-2367.

Brand, U., Logan, A., Hiller, N., and Richardson, J., 2003, Geochemistry of modern brachiopods: applications and implications for oceanography and paleoceanography: Chemical Geology, v. 198, no. 3, p. 305-334.

Chen, B., Joachimski, M. M., Shen, S.-z., Lambert, L. L., Lai, X.-l., Wang, X.-d., Chen, J., and Yuan, D.-x., 2013, Permian ice volume and palaeoclimate history: Oxygen isotope proxies revisited: Gondwana Research, v. 24, no. 1, p. 77-89.

Cisterna, G., and Archbold, N., 2007, Spiriferoidea (brachiopoda) from the early Permian del Salto Formation of Argentina: Alcheringa, v. 31, no. 1, p. 3-16.

Crowley, T. J., and Baum, S. K., 1992, Modeling late Paleozoic glaciation: Geology, v. 20, no. 6, p. 507-510.

Fielding, C. R., Frank, T. D., Birgenheier, L. P., Rygel, M. C., Jones, A. T., and Roberts, J., 2008, Stratigraphic imprint of the Late Palaeozoic Ice Age in eastern Australia: a record of alternating glacial and nonglacial climate regime: Journal of the Geological Society, v. 165, no. 1, p. 129-140.

Flake, R. C., 2011, Circulation of North American epicontinental seas during the Carboniferous using stable isotope and trace element analyses of brachiopod shells: Texas, Texas A&M University

Fürsich, F. T. and J. M. Hurst, 1980. Euryhalinity of Palaeozoic articulate brachiopods: Lethaia 13(4): 303-312.

Ghosh, P., Adkins, J., Affek, H., Balta, B., Guo, W., Schauble, E. A., Schrag, D., and Eiler, J. M., 2006, 13 C–18 O bonds in carbonate minerals: A new kind of paleothermometer: Geochimica et Cosmochimica Acta, v. 70, no. 6, p. 1439-1456.

Gonzalez, L. A., and Lohmann, K. C., 1985, Carbon and oxygen isotopic composition of Holocene reefal carbonates: Geology, v. 13, no. 11, p. 811-814.

Grosssman, E. L., 2019, Personal Communication, Texas A&M University

Grossman, E. L., 2012, Applying oxygen isotope paleothermometry in deep time: The Paleontological Society Papers, v. 18, p. 39-68.

Grossman, E. L., Yancey, T. E., Jones, T. E., Bruckschen, P., Chuvashov, B., Mazzullo, S. J., and Mii, H.-s., 2008, Glaciation, aridification, and carbon sequestration in the Permo-Carboniferous: the isotopic record from low latitudes: Palaeogeography, Palaeoclimatology, Palaeoecology, v. 268, no. 3, p. 222-233.

Haig, D. W., McCartain, E., Mory, A. J., Borges, G., Davydov, V. I., Dixon, M., Ernst, A., Groflin, S., Håkansson, E., Keep, M., Santos, Z. D., Shi, G. R., and Soares, J., 2014, Postglacial Early Permian (late Sakmarian–early Artinskian) shallow-marine carbonate deposition along a 2000km transect from Timor to west Australia: Palaeogeography, Palaeoclimatology, Palaeoecology, v. 409, no. Supplement C, p. 180-204.

Hays, J. D., Imbrie, J., and Shackleton, N. J., 1976, Variations in the Earth's orbit: pacemaker of the ice ages: American Association for the Advancement of Science Washington, DC.

Hays, P. D., and Grossman, E. L., 1991, Oxygen isotopes in meteoric calcite cements as indicators of continental paleoclimate: Geology, v. 19, no. 5, p. 441-444.

Henkes, G. A., Passey, B. H., Grossman, E. L., Shenton, B. J., Yancey, T. E., and Pérez-Huerta, A., 2018, Temperature evolution and the oxygen isotope composition of Phanerozoic oceans from carbonate clumped isotope thermometry: Earth and Planetary Science Letters, v. 490, p. 40-50.

Horton, D. E., Poulsen, C. J., Montañez, I. P., and DiMichele, W. A., 2012, Eccentricity-paced late Paleozoic climate change: Palaeogeography, Palaeoclimatology, Palaeoecology, v. 331, p. 150-161.

Horton, D. E., Poulsen, C. J., and Pollard, D., 2007, Orbital and CO2 forcing of late Paleozoic continental ice sheets: Geophysical Research Letters, v. 34, no. 19.

Hyde, W. T., Crowley, T. J., Tarasov, L., and Peltier, W. R., 1999, The Pangean ice age: Studies with a coupled climate-ice sheet model: Climate Dynamics, v. 15, no. 9, p. 619-629.

Ivany, L., and Runnegar, B., 2010, Early Permian seasonality from bivalve δ18O and implications for the oxygen isotopic composition of seawater: Geology, v. 38, no. 11, p. 1027-1030.

Korte, C., Jones, P. J., Brand, U., Mertmann, D., and Veizer, J., 2008, Oxygen isotope values from high-latitudes: clues for Permian sea-surface temperature gradients and Late Palaeozoic deglaciation: Palaeogeography, Palaeoclimatology, Palaeoecology, v. 269, no. 1, p. 1-16.

Kutzbach, J. and R. Gallimore, 1989, "Pangaean climates: megamonsoons of the megacontinent." Journal of Geophysical Research: Atmospheres 94(D3): 3341-3357.

Laya, J. C., Tucker, M. E., Gröcke, D. R., and Perez-Huerta, A., 2013a, Carbon, oxygen and strontium isotopic composition of low-latitude Permian carbonates (Venezuelan Andes): climate proxies of tropical Pangea: Geological Society, London, Special Publications, v. 376, p. SP376. 310.

Laya, J. C., Tucker, M. E., and Perez-Huerta, A., 2013b, Metre-scale cyclicity in Permian ramp carbonates of equatorial Pangea (Venezuelan Andes): Implications for sedimentation under tropical Pangea conditions: Sedimentary Geology, v. 292, p. 15-35.

Lear, C., Elderfield, H., and Wilson, P., 2000, Cenozoic deep-sea temperatures and global ice volumes from Mg/Ca in benthic foraminiferal calcite: Science, v. 287, no. 5451, p. 269-272.

Machel, H.-G., 1985, Cathodoluminescence in calcite and dolomite and its chemical interpretation: Geoscience Canada, v. 12, no. 4.

Mii, H.-S., and Grossman, E. L., 1994, Late Pennsylvanian seasonality reflected in the 18O and elemental composition of a brachiopod shell: Geology, v. 22, no. 7, p. 661-664.

Mii, H.-s., Grossman, E. L., and Yancey, T. E., 1997, Stable carbon and oxygen isotope shifts in Permian seas of West Spitsbergen-Global change or diagenetic artifact?: Geology, v. 25, no. 3, p. 227-230.

Mii, H. S., Grossman, E. L., and Yancey, T. E., 1999, Carboniferous isotope stratigraphies of North America: Implications for Carboniferous paleoceanography and Mississippian glaciation: Geological Society of America Bulletin, v. 111, no. 7, p. 960-973.

Montañez, I. P., and Poulsen, C. J., 2013, The Late Paleozoic Ice Age: An Evolving Paradigm: Annual Review of Earth and Planetary Sciences, v. 41, no. 1, p. 629-656.

Montañez, I. P., Tabor, N. J., Niemeier, D., DiMichele, W. A., Frank, T. D., Fielding, C. R., Isbell, J. L., Birgenheier, L. P., and Rygel, M. C., 2007, CO2-forced climate and vegetation instability during Late Paleozoic deglaciation: Science, v. 315, no. 5808, p. 87-91.

O'Neil, J. R., Clayton, R. N., and Mayeda, T. K., 1969, Oxygen isotope fractionation in divalent metal carbonates: The Journal of Chemical Physics, v. 51, no. 12, p. 5547-5558.

Pucéat, E., Reynard, B., and Lécuyer, C., 2004, Can crystallinity be used to determine the degree of chemical alteration of biogenic apatites?: Chemical Geology, v. 205, p. 83-97.

Reid, C. M., James, N. P., Beauchamp, B., and Kyser, T. K., 2007, Faunal turnover and changing oceanography: Late Palaeozoic warm-to-cool water carbonates, Sverdrup Basin, Canadian Arctic Archipelago: Palaeogeography, Palaeoclimatology, Palaeoecology, v. 249, no. 1, p. 128-159.

Richard, Z. D., et al. (2018). "Anomalously low δ18O values of high-latitude Permo-Triassic paleosol siderite." Palaeogeography, Palaeoclimatology, Palaeoecology 492: 26-40.

Roark, A., Flake, R., Grossman, E. L., Olszewski, T., Lebold, J., Thomas, D., Marcantonio, F., Miller, B., Raymond, A., and Yancey, T., 2017, Brachiopod geochemical records from across the Carboniferous seas of North America: Evidence for salinity gradients, stratification, and circulation patterns: Palaeogeography, Palaeoclimatology, Palaeoecology, v. 485, p. 136-153.

Roark, A., Grossman, E. L., and Lebold, J., 2016, Low seasonality in central equatorial Pangea during a late Carboniferous highstand based on high-resolution isotopic records of brachiopod shells: Geological Society of America Bulletin, v. 128.

Roberts, C. D., LeGrande, A. N., and Tripati, A. K., 2011, Sensitivity of seawater oxygen isotopes to climatic and tectonic boundary conditions in an early Paleogene simulation with GISS ModelE-R: Paleoceanography, v. 26, no. 4.

Romanin, M., Crippa, G., Ye, F., Brand, U., Bitner, M. A., Gaspard, D., Häussermann, V., and Laudien, J., 2018, A sampling strategy for recent and fossil brachiopods: selecting the optimal shell segment for geochemical analyses: Rivista Italiana di Paleontologia e Stratigrafia (Research In Paleontology and Stratigraphy), v. 124, no. 2.

Saltzman, M. R., 2002, Carbon and oxygen isotope stratigraphy of the Lower Mississippian (Kinderhookian–lower Osagean), western United States: implications for seawater chemistry and glaciation: Geological Society of America Bulletin, v. 114, no. 1, p. 96-108.

Scotese, C., Boucot, A., and McKerrow, W., 1999, Gondwanan palaeogeography and pal1 oclimatology: Journal of African Earth Sciences, v. 28, no. 1, p. 99-114.

Tabor, N. J., and Poulsen, C. J., 2008, Palaeoclimate across the Late Pennsylvanian–Early Permian tropical palaeolatitudes: a review of climate indicators, their distribution, and relation to palaeophysiographic climate factors: Palaeogeography, Palaeoclimatology, Palaeoecology, v. 268, no. 3-4, p. 293-310.

Thompson, S. L., and Pollard, D., 1997, Greenland and Antarctic Mass Balances for Present and Doubled Atmospheric CO2 from the GENESIS Version-2 Global Climate Model: Journal of Climate, v. 10, no. 5, p. 871-900.

Yamamoto, K., Asami, R., and Iryu, Y., 2010, Within-shell variations in carbon and oxygen isotope compositions of two modern brachiopods from a subtropical shelf environment off Amami-o-shima, southwestern Japan: Geochemistry, Geophysics, Geosystems, v. 11, no. 10.

Zachos, J., Pagani, M., Sloan, L., Thomas, E., and Billups, K., 2001, Trends, rhythms, and aberrations in global climate 65 Ma to present: Science, v. 292, no. 5517, p. 686-693.

Zachos, J. C., Stott, L. D., and Lohmann, K. C., 1994, Evolution of early Cenozoic marine temperatures: Paleoceanography, v. 9, no. 2, p. 353-387.

Ziegler, A. M., 1997. "Permian world topography and climate." Late gracial and postgracial environmental changes-Quaternary, Carboniferous-Permian and Proterozoic: 1-37.

APPENDIX I

INDIVIDUAL SAMPLE IMAGES AND RECORDS

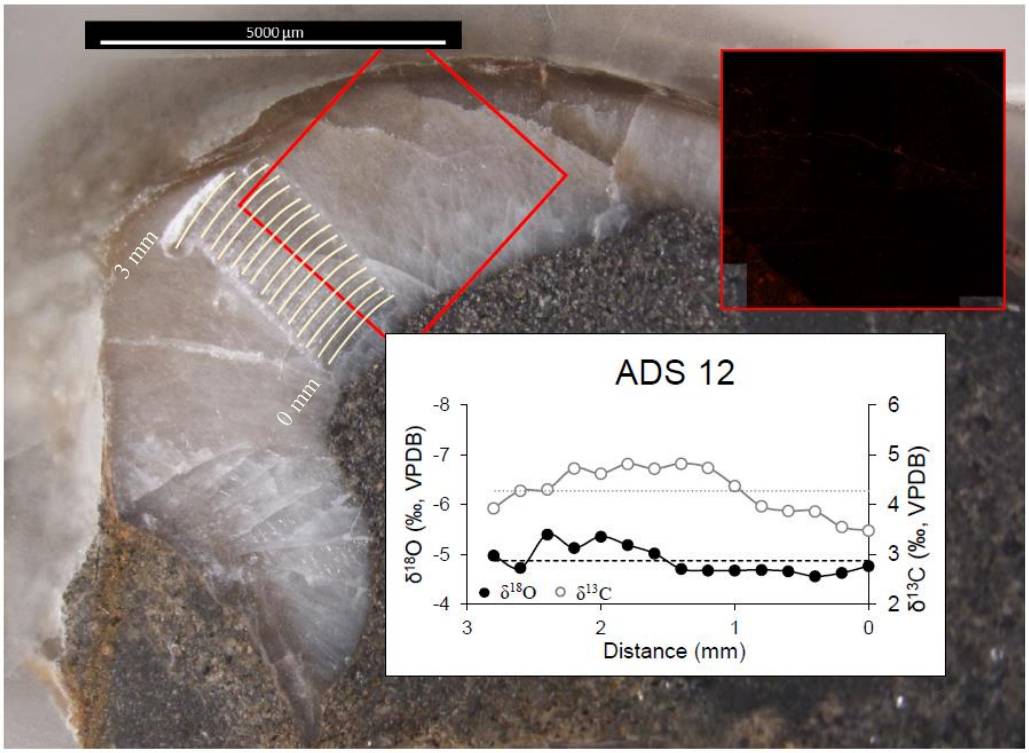

Figure A-1, Sample ADS 12

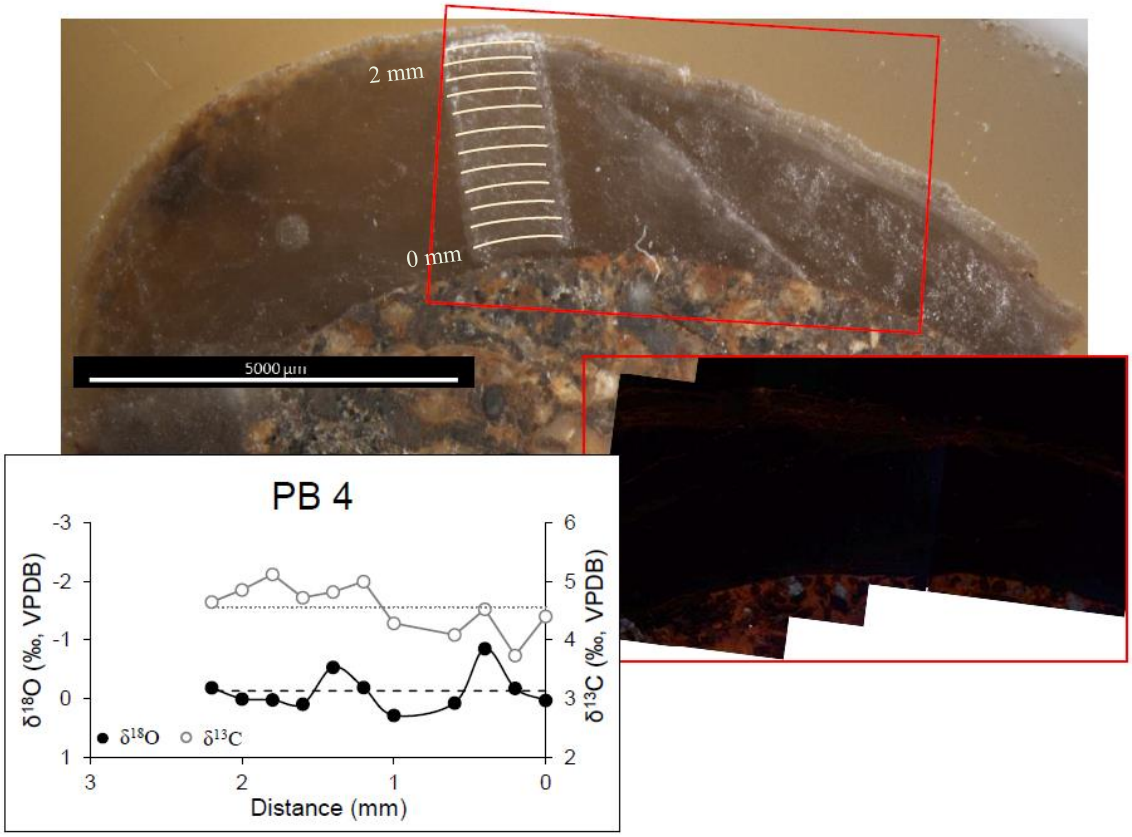

Figure A-2, Sample PB 4

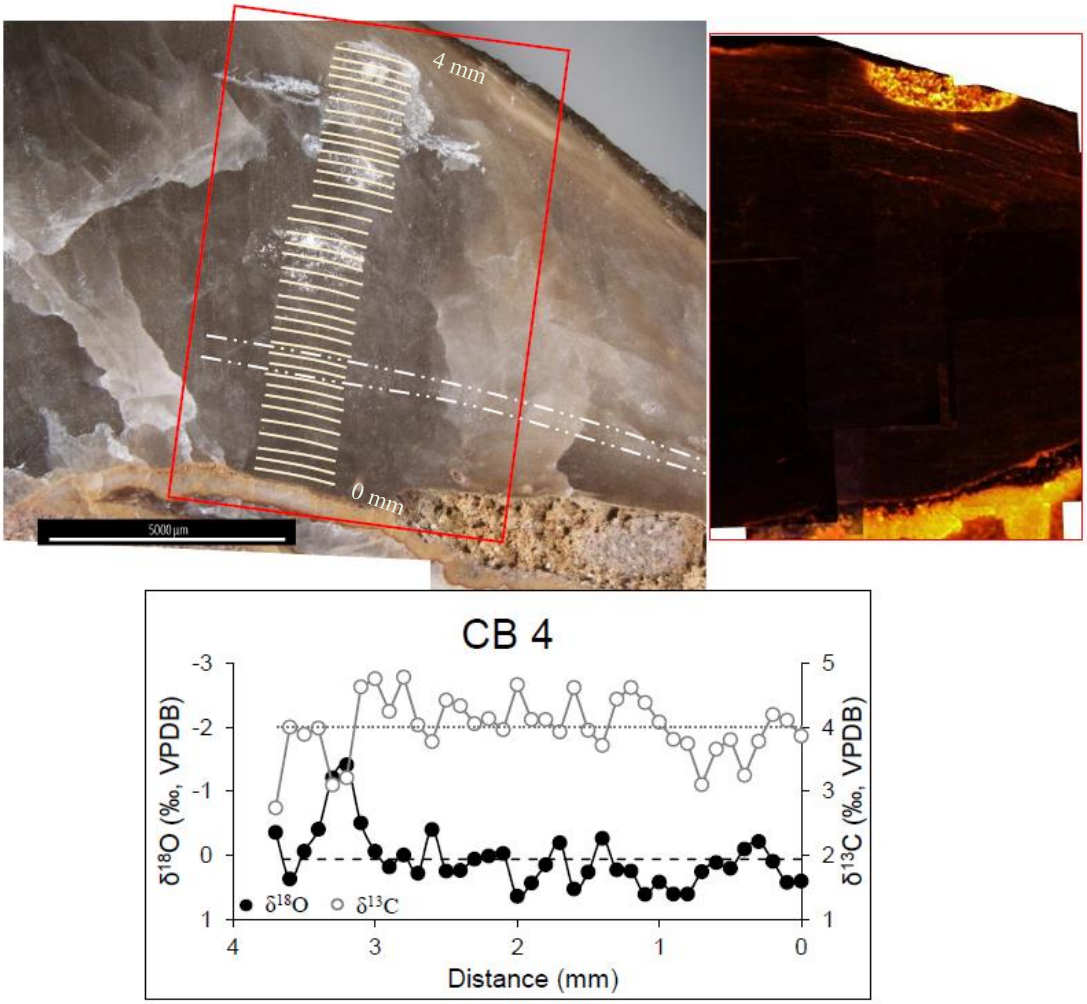

Figure A-3, Sample CB 4 Dotted lines indicate visible growth bands.

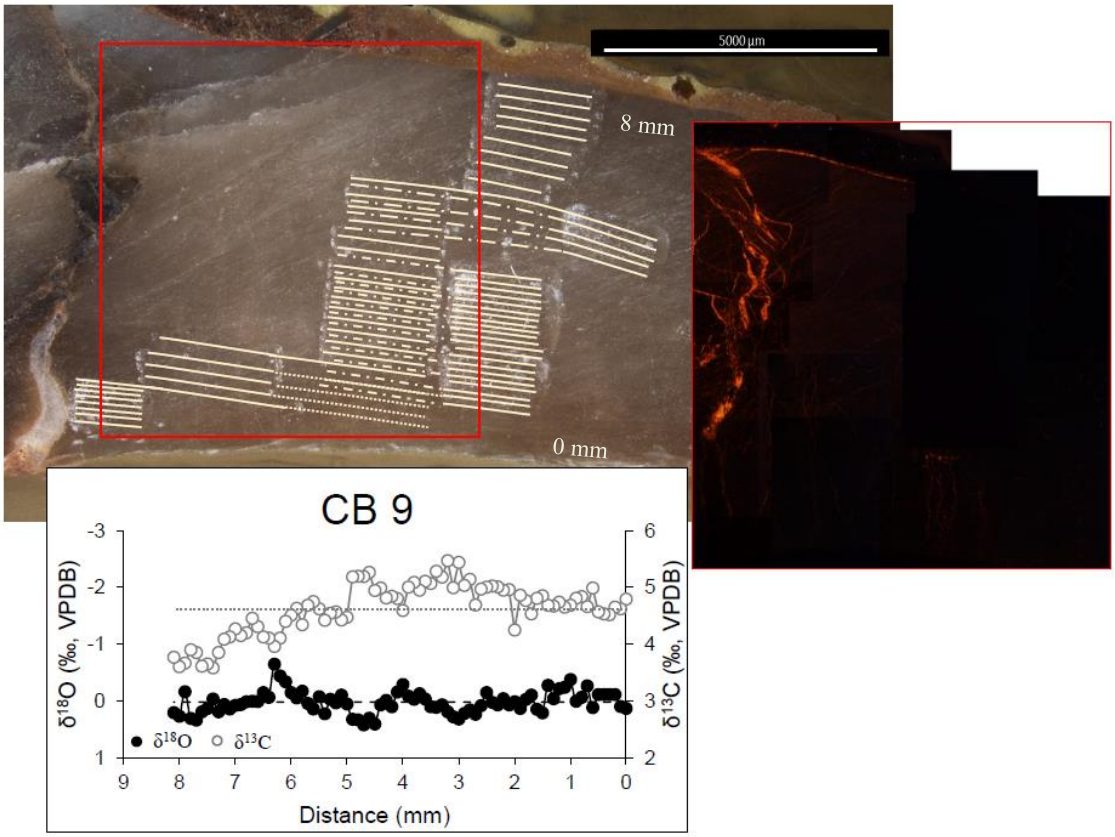

Figure A-4, Sample CB 9

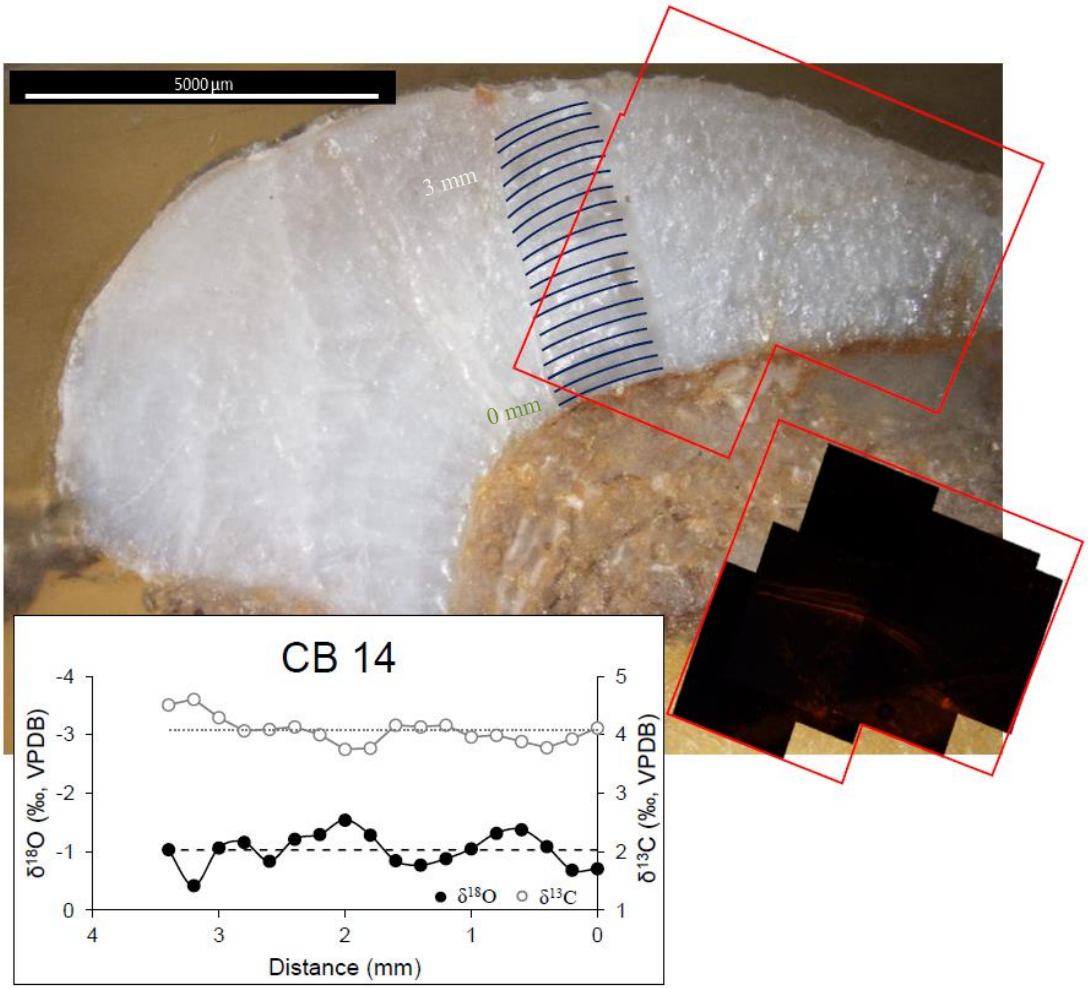

Figure A-5, Sample CB 14

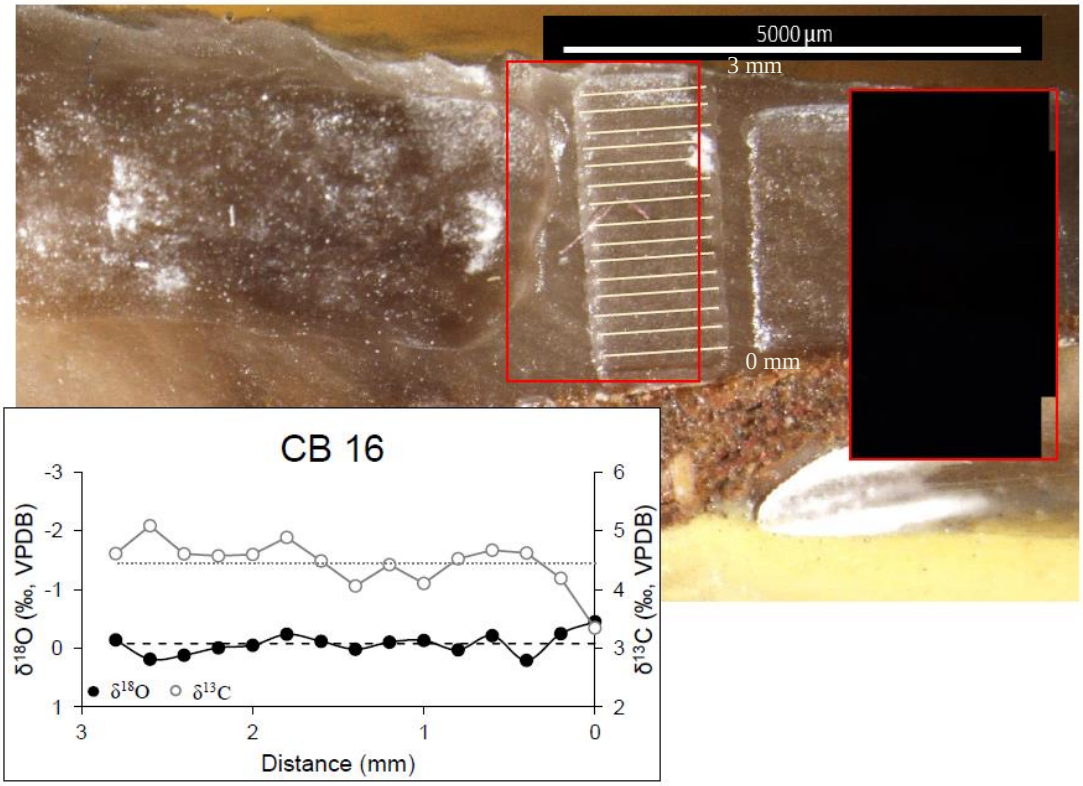

Figure A-6, Sample CB 16

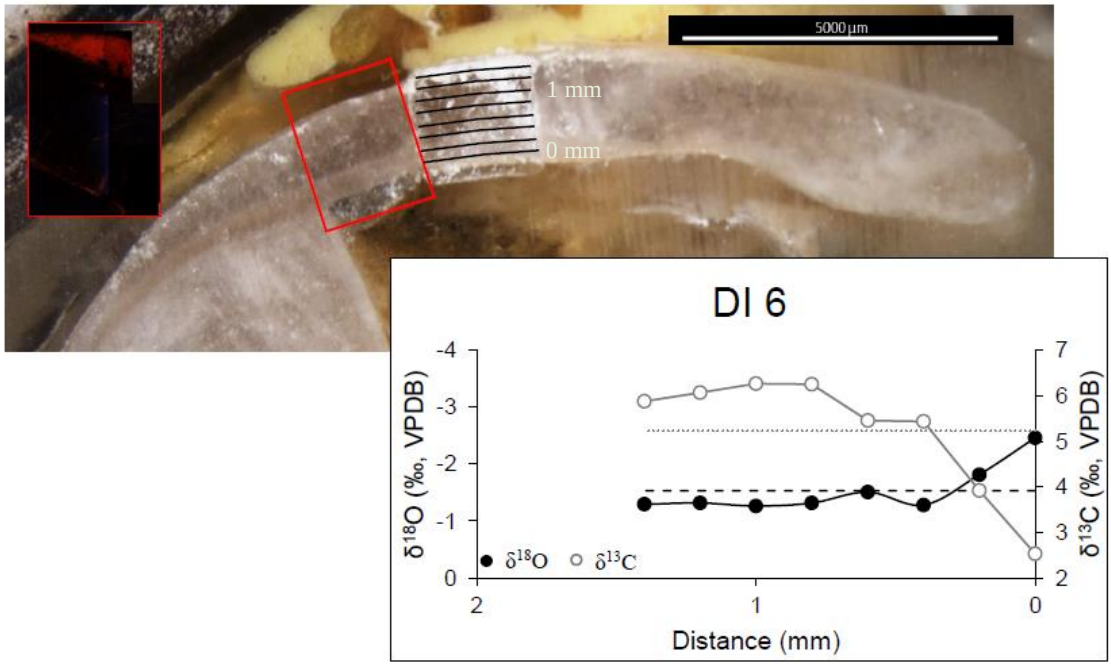

Figure A-7, Sample DI 6

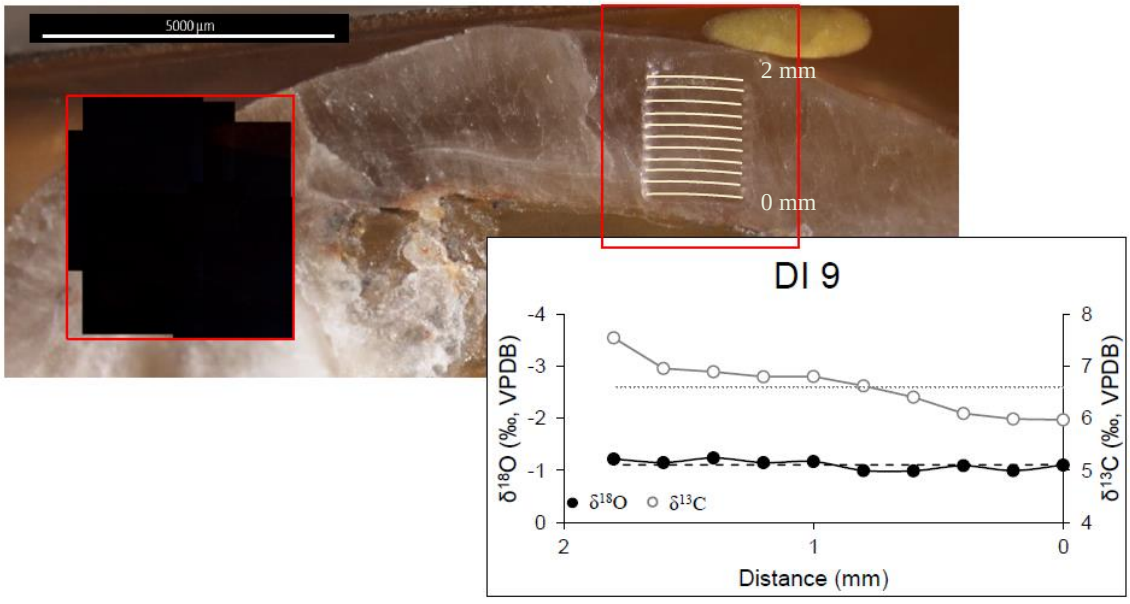

Figure A-8, Sample DI 9

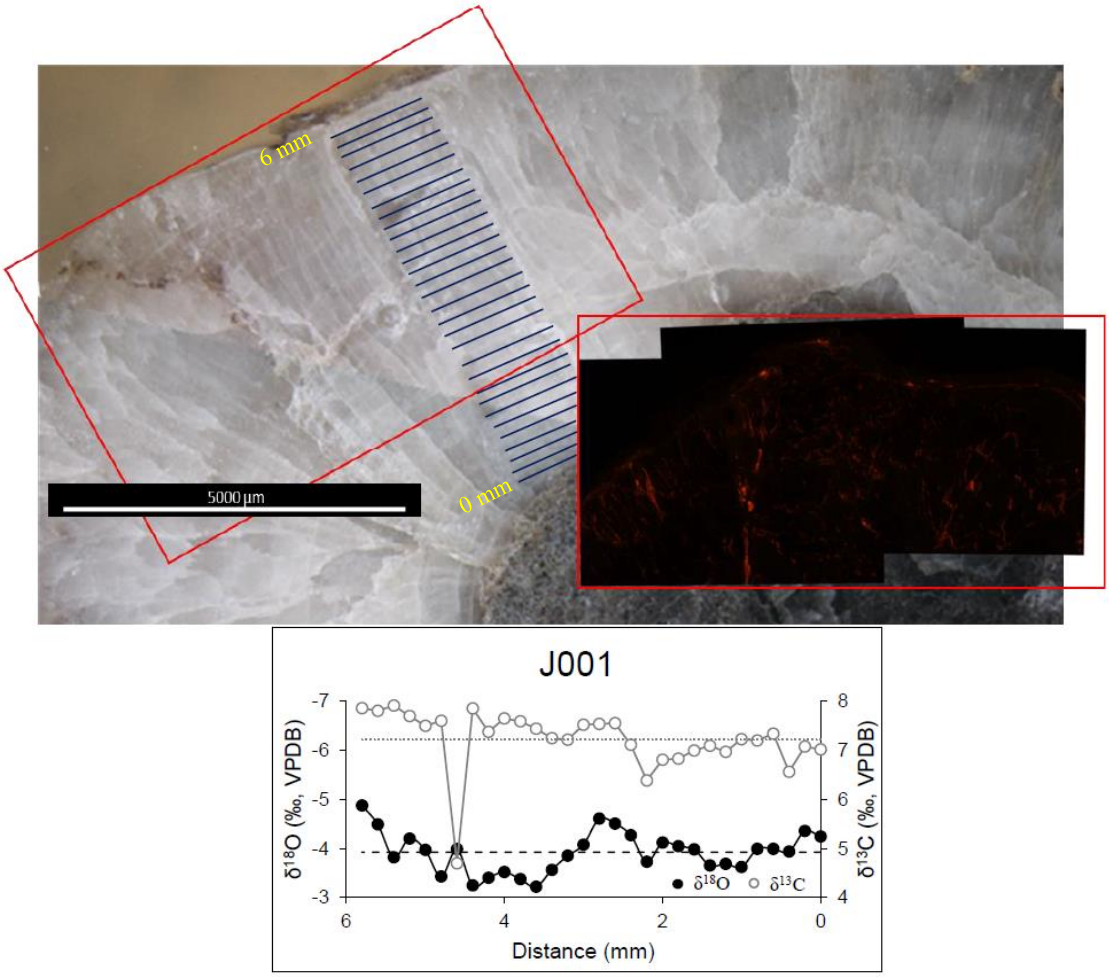

Figure A-9, Sample J001

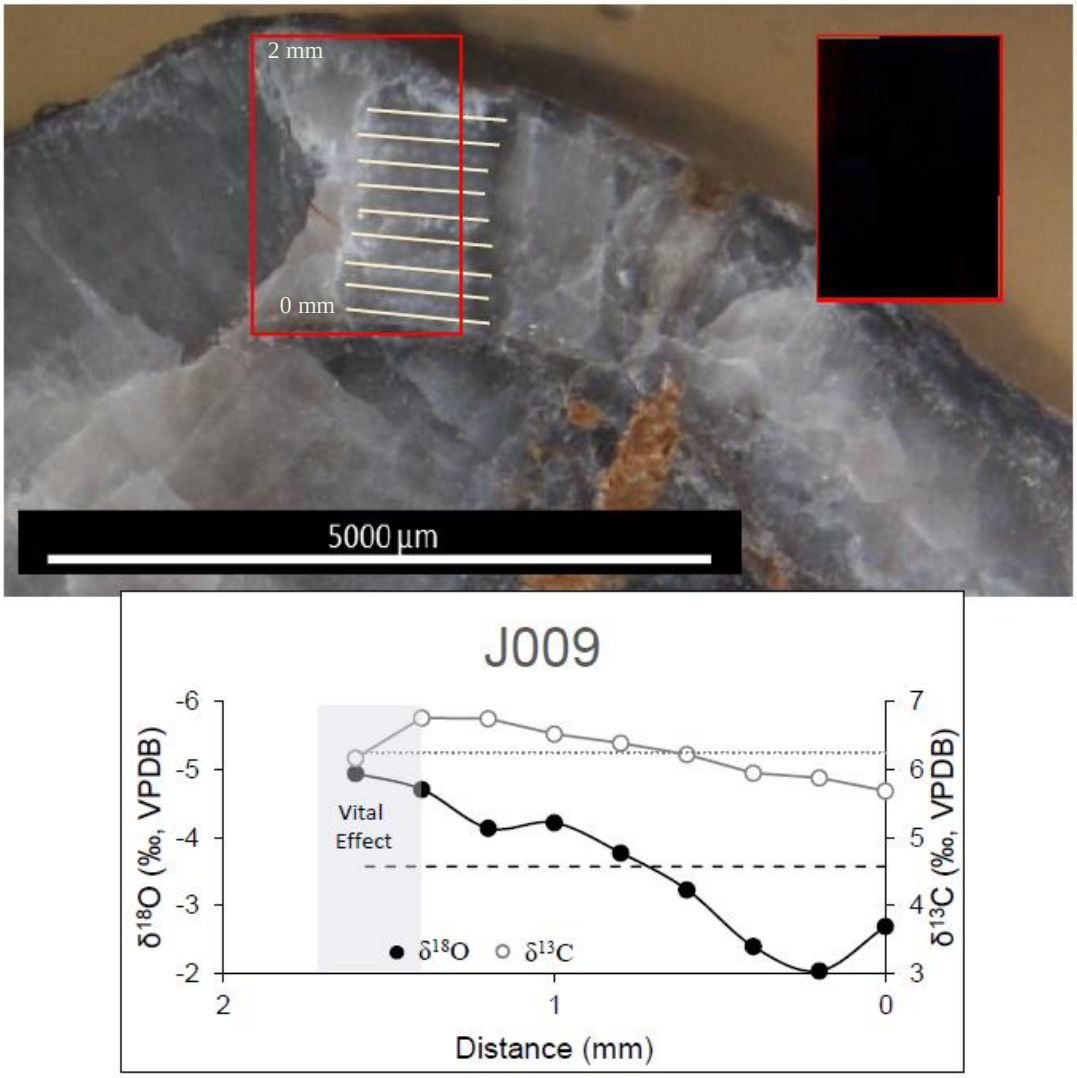

Figure A-10, Sample J009

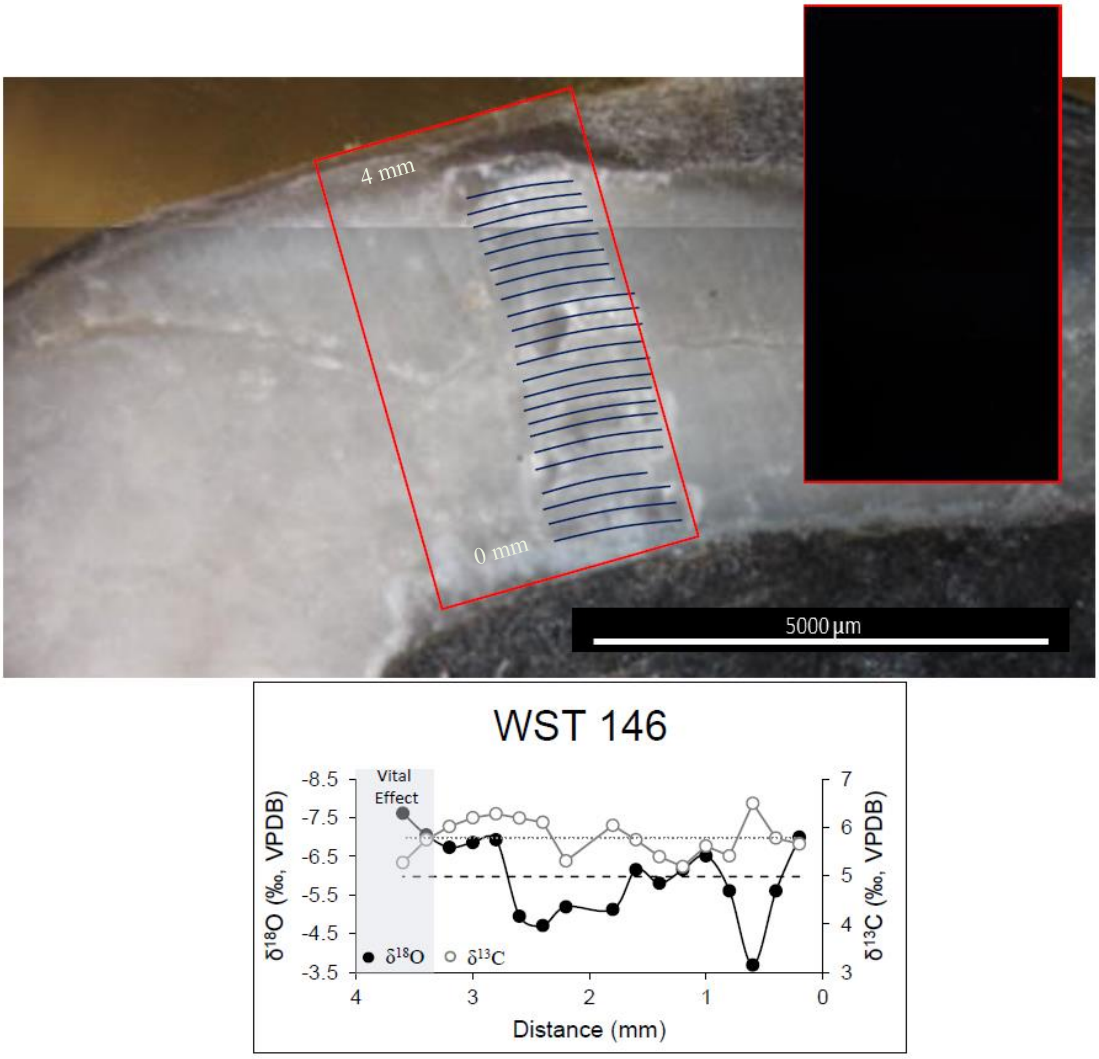

Figure A-11, Sample WST 146

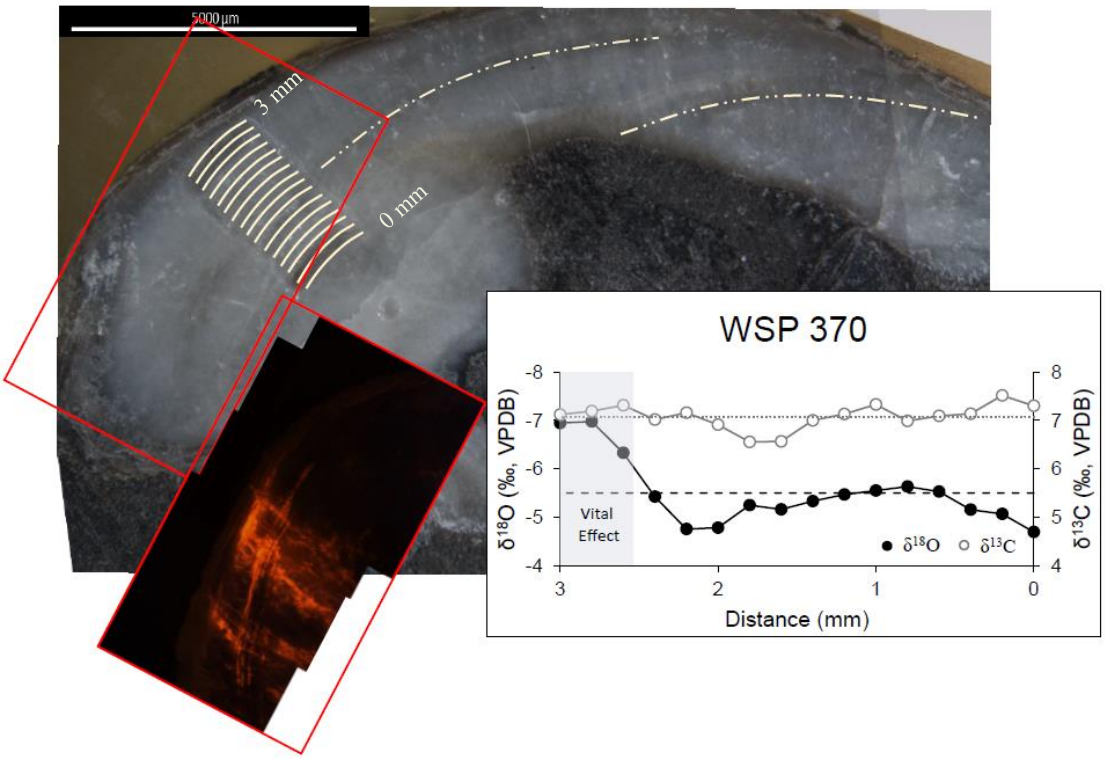

Figure A-12, Sample WSP 370; Dotted lines indicate visible growth bands.

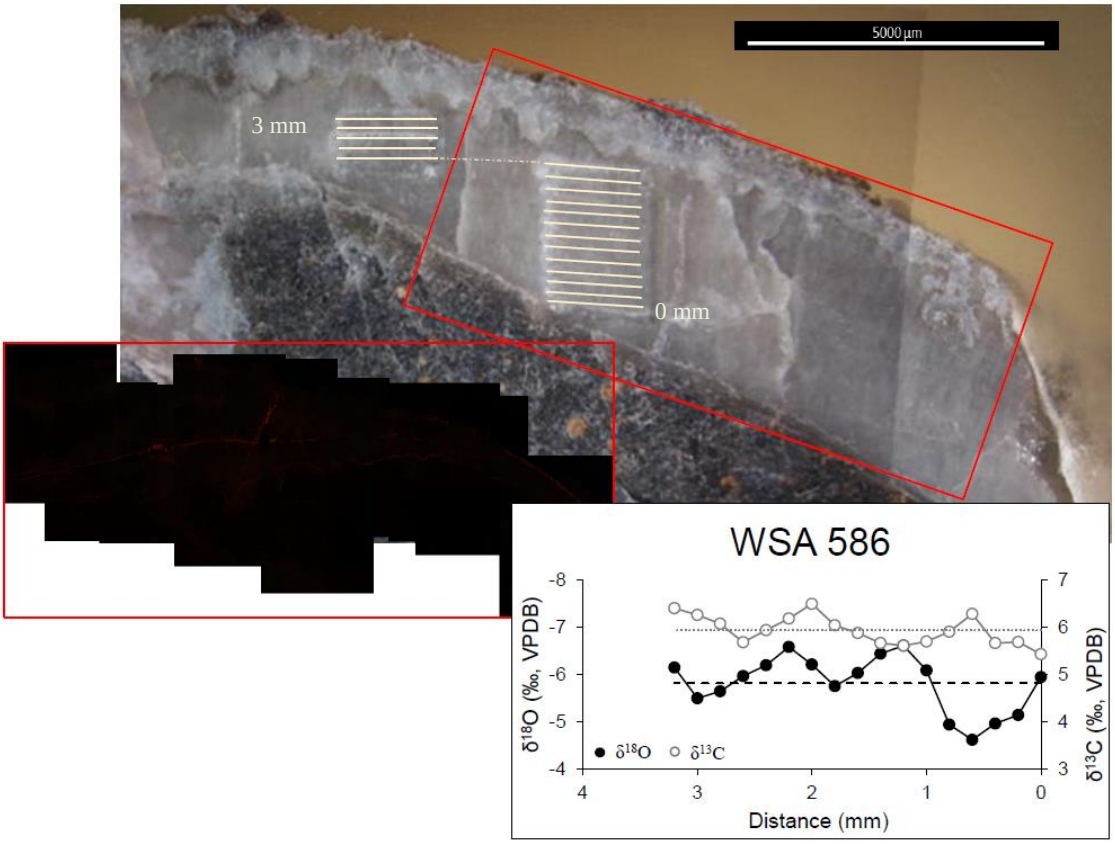

Figure A-13, Sample WSA 586

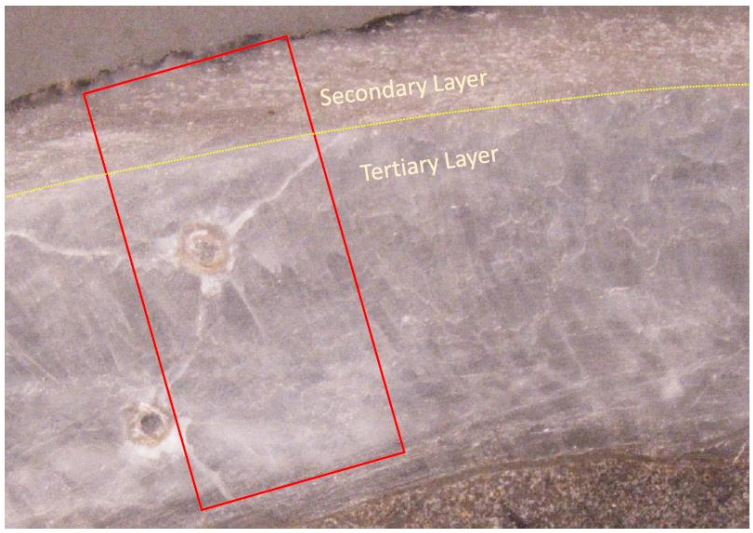

Figure A-14, sample WST 146 thin section. Sample area outlined by red box and figure shows that sampling occurred across a change in shell microstructure indicating change from prismatic to coarsely fibrous

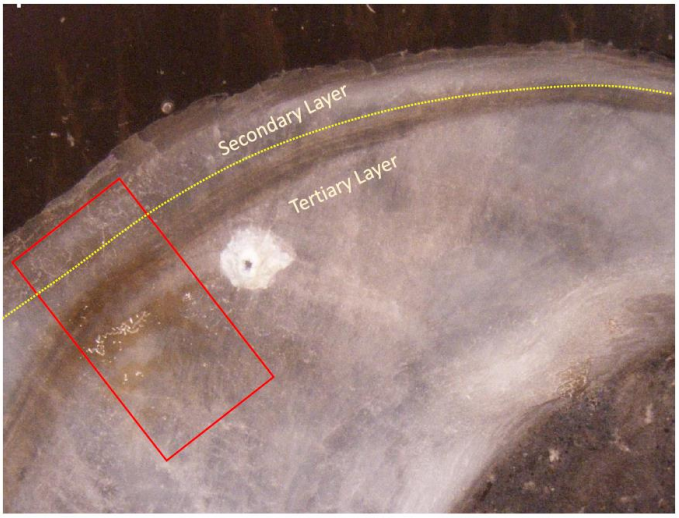

Figure A-15, sample WSP 370 thin section. Sample area outlined by red box and figure shows that sampling occurred across a change in shell microstructure indicating change from prismatic to coarsely fibrous

Figure A-16, sample J009 thin section. Sample area outlined by red box and figure shows that sampling occurred across a change in shell microstructure indicating change from prismatic to coarsely fibrous

APPENDIX II

Sample ID	Taxa	CL Character	*n*	*Dist. between points (mm)*	δ13C (‰, VPDB)	δ18O (‰, VPDB)
Svalbard						
J001	**Spiriferella polaris**	**NL**	**30**		**7.47**	**-3.92**
			1	0	7.27	-4.24
			2	0.2	7.33	-4.35
			3	0.4	6.81	-3.93
			4	0.6	7.59	-3.99
			5	0.8	7.45	-3.99
			6	1	7.47	-3.62
			7	1.2	7.22	-3.68
			8	1.4	7.34	-3.65
			9	1.6	7.24	-3.98
			10	1.8	7.08	-4.04
			11	2	7.06	-4.11
			12	2.2	6.63	-3.72
			13	2.4	7.36	-4.27
			14	2.6	7.80	-4.50
			15	2.8	7.78	-4.60
			16	3	7.77	-4.07
			17	3.2	7.46	-3.85
			18	3.4	7.50	-3.56
			19	3.6	7.69	-3.22
			20	3.8	7.84	-3.37
			21	4	7.90	-3.51
			22	4.2	7.62	-3.40
			23	4.4	8.10	-3.24
			24	4.6	4.94	-3.98
			25	4.8	7.85	-3.42
			26	5	7.75	-3.97
			27	5.2	7.95	-4.20
			28	5.4	8.16	-3.81
			29	5.6	8.06	-4.49
			30	5.8	8.11	-4.88
J009	**Spiriferella polaris**	**NL/SL**	**9**		**6.19**	**-3.21**
			1	0	5.68	-2.69
			2	0.2	5.87	-2.03

				3	0.4	5.94	-2.39
				4	0.6	6.22	-3.23
				5	0.8	6.38	-3.77
				6	1	6.52	-4.21
				7	1.2	6.74	-4.13
				8	1.4	6.75	-4.70
				9	1.6	6.16	-4.94
WST 146	**Spiriferella polaris**	**NL**	**23**			**5.82**	**-5.88**
				1	0		
				2	0.2	5.65	-6.99
				3	0.4	5.78	-5.60
				4	0.6	6.49	-3.69
				5	0.8	5.41	-5.61
				6	1	5.61	-6.51
				7	1.2	5.19	-6.15
				8	1.4	5.39	-5.80
				9	1.6	5.74	-6.15
				10	1.8	6.04	-5.13
				12	2.2	5.30	-5.19
				13	2.4	6.10	-4.71
				14	2.6	6.19	-4.95
				15	2.8	6.28	-6.92
				16	3	6.20	-6.85
				17	3.2	6.01	-6.73
				18	3.4	5.74	-7.05
				19	3.6	5.27	-7.61
WSP 370	**Spiriferella polaris**	**NL**	**16**			**7.06**	**-5.22**
				1	0	7.30	-4.70
				2	0.2	7.52	-5.07
				3	0.4	7.14	-5.16
				4	0.6	7.10	-5.53
				5	0.8	6.99	-5.63
				6	1	7.33	-5.55
				7	1.2	7.13	-5.47
				8	1.4	7.00	-5.33
				9	1.6	6.57	-5.16
				10	1.8	6.56	-5.25
				11	2	6.91	-4.78
				12	2.2	7.16	-4.75

			13	2.4	7.02	-5.43
			14	2.6	7.32	-6.33
			15	2.8	7.19	-6.98
			16	3	7.12	-6.95
WSA 586	**Cleiothyridina**	**NL**	**17**		**5.93**	**-5.81**
			1	0	5.43	-5.94
			2	0.2	5.68	-5.14
			3	0.4	5.66	-4.96
			4	0.6	6.27	-4.62
			5	0.8	5.90	-4.94
			6	1	5.69	-6.08
			7	1.2	5.60	-6.60
			8	1.4	5.66	-6.43
			9	1.6	5.87	-6.03
			10	1.8	6.03	-5.75
			11	2	6.49	-6.21
			12	2.2	6.17	-6.58
			13	2.4	5.93	-6.19
			14	2.6	5.68	-5.97
			15	2.8	6.07	-5.64
			16	3	6.25	-5.50
			17	3.2	6.39	-6.14
CB 4	**Imperiospira sp.**	**NL**	**38**		**4.00**	**0.06**
			1	0	3.86	0.41
			2	0.1	4.11	0.42
			3	0.2	4.20	0.10
			4	0.3	3.78	-0.21
			5	0.4	3.25	-0.10
			6	0.5	3.80	0.20
			7	0.6	3.66	0.12
			8	0.7	3.10	0.26
			9	0.8	3.74	0.60
			10	0.9	3.81	0.61
			11	1	4.08	0.42
			12	1.1	4.38	0.61
			13	1.2	4.62	0.25
			14	1.3	4.43	0.23
			15	1.4	3.71	-0.26
			16	1.5	3.95	0.26
			17	1.6	4.62	0.53

			18	1.7	3.93	-0.19
			19	1.8	4.11	0.15
			20	1.9	4.12	0.43
			21	2	4.66	0.64
			22	2.1	3.96	-0.03
			23	2.2	4.13	0.01
			24	2.3	4.05	0.06
			25	2.4	4.33	0.24
			26	2.5	4.42	0.25
			27	2.6	3.77	-0.40
			28	2.7	4.03	0.28
			29	2.8	4.78	0.00
			30	2.9	4.24	0.18
			31	3	4.76	-0.06
			32	3.1	4.63	-0.50
			33	3.2	3.21	-1.41
			34	3.3	3.10	-1.21
			35	3.4	3.98	-0.40
			36	3.5	3.89	-0.06
			37	3.6	4.00	0.37
			38	3.7	2.74	-0.36
CB 9	**Myodelthyrium sp.**	**NL**	**82**		**4.61**	**0.02**
			1	0	4.79	0.13
			2	0.1	4.62	0.10
			3	0.2	4.65	-0.11
			4	0.3	4.52	-0.11
			5	0.4	4.53	-0.11
			6	0.5	4.57	-0.11
			7	0.6	4.99	0.12
			8	0.7	4.66	-0.26
			9	0.8	4.84	-0.06
			10	0.9	4.80	0.01
			11	1	4.68	-0.38
			12	1.1	4.65	-0.24
			13	1.2	4.74	-0.21
			14	1.3	4.67	-0.04
			15	1.4	4.68	-0.27
			16	1.5	4.85	0.21
			17	1.6	4.81	0.15

18	1.7	4.53	-0.10
19	1.8	4.76	-0.02
20	1.9	4.86	0.13
21	2	4.25	0.02
22	2.1	4.96	0.07
23	2.2	4.95	-0.04
24	2.3	5.01	0.07
25	2.4	5.02	0.03
26	2.5	5.00	-0.14
27	2.6	4.97	0.08
28	2.7	4.69	0.24
29	2.8	5.14	0.16
30	2.9	5.03	0.22
31	3	5.44	0.32
32	3.1	4.99	0.28
33	3.2	5.47	0.19
34	3.3	5.18	0.07
35	3.4	5.28	0.11
36	3.5	5.07	0.10
37	3.6	5.11	-0.03
38	3.7	4.95	-0.12
39	3.8	5.08	-0.03
40	3.9	5.00	-0.08
41	4	4.59	-0.29
42	4.1	4.80	-0.16
43	4.2	4.84	0.11
44	4.3	4.81	-0.01
45	4.4	4.99	0.07
46	4.5	4.94	0.41
47	4.6	5.26	0.30
48	4.7	5.19	0.42
49	4.8	5.19	0.33
50	4.9	5.18	0.32
51	5	4.47	0.05
52	5.1	4.42	-0.10
53	5.2	4.57	0.04
54	5.3	4.54	-0.03
55	5.4	4.42	0.23
56	5.5	4.62	-0.07
57	5.6	4.74	0.14

			58	5.7	4.68	0.05
			59	5.8	4.34	-0.17
			60	5.9	4.63	-0.05
			61	6	4.51	-0.15
			62	6.1	4.40	-0.34
			63	6.2	4.10	-0.44
			64	6.3	3.96	-0.65
			65	6.4	4.10	-0.06
			66	6.5	4.12	-0.15
			67	6.6	4.31	0.01
			68	6.7	4.45	0.01
			69	6.8	4.20	0.02
			70	6.9	4.15	0.06
			71	7	4.27	0.08
			72	7.1	4.12	0.14
			73	7.2	4.09	0.07
			74	7.3	3.85	0.19
			75	7.4	3.58	-0.03
			76	7.5	3.65	0.13
			77	7.6	3.61	0.19
			78	7.7	3.85	0.34
			79	7.8	3.90	0.31
			80	7.9	3.66	-0.16
			81	8	3.60	0.27
			82	8.1	3.77	0.21
CB 14	**Elivina hoskinga**	**CL**	**18**		**4.08**	**-1.03**
			1	0	4.11	-0.71
			2	0.2	3.93	-0.69
			3	0.4	3.78	-1.09
			4	0.6	3.89	-1.38
			5	0.8	3.99	-1.32
			6	1	3.96	-1.05
			7	1.2	4.16	-0.88
			8	1.4	4.13	-0.78
			9	1.6	4.17	-0.85
			10	1.8	3.77	-1.29
			11	2	3.75	-1.54
			12	2.2	4.00	-1.30
			13	2.4	4.14	-1.22
			14	2.6	4.09	-0.84

			15	2.8	4.07	-1.16
			16	3	4.29	-1.07
			17	3.2	4.61	-0.42
			18	3.4	4.51	-1.04
CB 16	**Myodelthyrium**	**NL**	**15**		**4.45**	**-0.08**
			1	0	3.34	-0.45
			2	0.2	4.19	-0.25
			3	0.4	4.62	0.21
			4	0.6	4.67	-0.21
			5	0.8	4.53	0.03
			6	1	4.10	-0.13
			7	1.2	4.42	-0.10
			8	1.4	4.06	0.02
			9	1.6	4.49	-0.12
			10	1.8	4.89	-0.24
			11	2	4.60	-0.05
			12	2.2	4.58	-0.01
			13	2.4	4.61	0.12
			14	2.6	5.08	0.19
			15	2.8	4.61	-0.14
PB 4	**Spirelytha fredericksi**	**NL**	**12**		**4.56**	**-0.13**
			1	0	4.40	0.03
			2	0.2	3.73	-0.17
			3	0.4	4.52	-0.85
			4	0.6	4.09	0.08
			6	1	4.28	0.29
			7	1.2	5.00	-0.19
			8	1.4	4.82	-0.53
			9	1.6	4.72	0.09
			10	1.8	5.12	0.02
			11	2	4.85	0.01
			12	2.2	4.65	-0.18
DI 6	**Spiriferella sp.**	**NL**	**8**		**5.22**	**-1.53**
			1	0	2.53	-2.46
			2	0.2	3.92	-1.81
			3	0.4	5.43	-1.28
			4	0.6	5.45	-1.51
			5	0.8	6.24	-1.32
			6	1	6.26	-1.26

			7	1.2	6.06	-1.32
			8	1.4	5.87	-1.29
DI 9	**Neospirifer sp.**	**NL**	**11**		**6.61**	**-1.11**
			1	0	5.98	-1.10
			2	0.2	5.99	-0.99
			3	0.4	6.09	-1.09
			4	0.6	6.41	-0.99
			5	0.8	6.63	-1.00
			6	1	6.81	-1.17
			7	1.2	6.80	-1.15
			8	1.4	6.90	-1.24
			9	1.6	6.96	-1.15
			10	1.8	7.55	-1.22
ADS 12	**Pericospira Sanjuanesis**	**NL**	**15**		**4.27**	**-4.87**
			1	0	3.47	-4.76
			2	0.2	3.55	-4.62
			3	0.4	3.86	-4.56
			4	0.6	3.87	-4.66
			5	0.8	3.96	-4.68
			6	1	4.37	-4.67
			7	1.2	4.74	-4.68
			8	1.4	4.82	-4.70
			9	1.6	4.72	-5.02
			10	1.8	4.81	-5.18
			11	2	4.62	-5.35
			12	2.2	4.72	-5.13
			13	2.4	4.30	-5.40
			14	2.6	4.28	-4.72
			15	2.8	3.92	-4.98